REPORT DOCUMENTATION PAGE

AFRL-SR-BL-TR-00-

0017

ng

Public Reporting burden for this collection of information is estimated to average 1 hour per response, including the time and maintaining the data needed, and completing and reviewing the collection of information. Send comment regarding information, including suggestions for reducing this burden, to Washington Headquarters Services, Directorate for inform 1204, Arlington, VA 22202-4302, and to the Office of Management and Budget, Paperwork Reduction Project (0704-0188,) Washington, DC 20503.

1. AGENCY USE ONLY (Leave Blank)	2. REPORT DATE 21 SEP 99	3. REPORT TYPE AND DATES COVERED Final, 23 Feb 98 – 31 Jul 99
4. TITLE AND SUBTITLE Scintillation control for adaptive optical sensors		5. FUNDING NUMBERS Contract Number F49620-98-1-0295
6. AUTHOR(S) Michael C. Roggemann		
7. PERFORMING ORGANIZATION NAME(S) AND ADDRESS(ES) Michigan Technological University		8. PERFORMING ORGANIZATION REPORT NUMBER
9. SPONSORING / MONITORING AGENCY NAME(S) AND ADDRESS(ES) U. S. Air Force Office of Scientific Research/NM 110 Duncan Ave., Room B115 Bolling AFB, DC 20332-8050		10. SPONSORING / MONITORING AGENCY REPORT NUMBER

11. SUPPLEMENTARY NOTES
    The views and conclusions contained in this report are those of the author(s) and should not be iinterpreted as necessarily representing the official policies or endorsements, either expressed or implied, of the Air Force Office of Scientific Research or the US Government.

12 a. DISTRIBUTION / AVAILABILITY STATEMENT Approved for public release; distribution unlimited.	12 b. DISTRIBUTION CODE

13. ABSTRACT (Maximum 200 words)

Michigan Technological University (MTU) has been investigating strategies for overcoming the effects of scintillation on adaptive optical imaging and laser beam projection systems which must operate in the presence of extended path turbulence. The approach originally proposed under this contract involved using two deformable mirrors to fully conjugate the received or transmitted beam. Our investigations into this concept have shown that implementation details associated with the use of real adaptive optical hardware will likely limit the effectiveness of the two deformable mirror technique. As a consequence, an alternative approach using one deformable mirror was developed, and its performance was investigated. This technique exploits the fact that, under strong scintillation conditions, information about the phase of the beacon field is incorporated in the intensity of the beacon field. Hence, deformable mirror commands which are consistent with all of the intensity measurements available to an adaptive optical system are processed using a new nonlinear optimization-based algorithm. Our studies of the performance of this technique have shown that under conditions of saturated scintillation this new approach significantly outperforms the standard centroid-based processing of the Hartmann sensor measurements. An experiment conducted at MTU has demonstrated the ability to predict a laser intensity pattern in a distant target plane using Hartmann sensor measurements of the field reflected from a deformable mirror. One accepted journal article, and one submitted journal article have resulted from this work, along with three conference papers. In addition, this work forms the basis of a program which is now being conducted with the Airborne Laser Technology Division.

14. SUBJECT TERMS			15. NUMBER OF PAGES 58
			16. PRICE CODE

17. SECURITY CLASSIFICATION OR REPORT **UNCLASSIFIED**	18. SECURITY CLASSIFICATION ON THIS PAGE **UNCLASSIFIED**	19. SECURITY CLASSIFICATION OF ABSTRACT **UNCLASSIFIED**	20. LIMITATION OF ABSTRACT UL

NSN 7540-01-280-5500

Standard Form 298 (Rev.2-89)
Prescribed by ANSI Std. 239-18
298-102

20000121 018

DTIC QUALITY INSPECTED 1

Final Report on "Scintillation control for adaptive optical sensors", Contract Number F49620-98-1-0295

Michael C. Roggemann [*]

Abstract

Michigan Technological University (MTU), under contract to the Air Force Office of Scientific Research (AFOSR), has been investigating strategies for overcoming the effects of scintillation on adaptive optical imaging and laser beam projection systems which must operate in the presence of extended path turbulence. The approach originally proposed under this contract involved using two deformable mirrors to fully conjugate the received or transmitted beam. Our investigations into this concept have shown that implementation details associated with the use of real adaptive optical hardware will likely limit the effectiveness of the two deformable mirror technique. As a consequence, an alternative approach using one deformable mirror was developed, and its performance was investigated. This technique exploits the fact that, under strong scintillation conditions, information about the *phase* of the beacon field is incorporated in the *intensity* of the beacon field. Hence, deformable mirror commands which are consistent with all of the intensity measurements available to an adaptive optical system are processed using a new nonlinear optimization-based algorithm. Our studies of the performance of this technique have shown that under conditions of saturated scintillation this new approach significantly outperforms the standard centroid-based processing of the Hartmann sensor measurements. An experiment conducted at MTU has demonstrated the ability to predict a laser intensity pattern in a distant target plane using Hartmann sensor measurements of the field reflected from a deformable mirror. One accepted journal article, and

[*]Michigan Technological University, Department of Electrical Engineering, 1400 Townsend Drive, Houghton, Michigan 49931, e-mail: mroggema@mtu.edu, phone: (906) 487-2164

1

one submitted journal article have resulted from this work, along with three conference papers. In addition, this work forms the basis of a program which is now being conducted with the Airborne Laser Technology Division.

1   Introduction.

Atmospheric turbulence corrupts propagating optical wave fronts. If the turbulence lies outside the near field region of the aperture both the phase and the amplitude of the wave are corrupted at the receiver [1, 2]. The problem of correcting for the phase effects of atmospheric turbulence has received a great deal of attention in the literature [3, 4]. Adaptive optical systems which can effectively conjugate the phase of a wave front corrupted by near field turbulence, where turbulence-induced phase effects dominate the atmospheric degradation of performance, are becoming mature [5]. As adaptive optical systems continue to develop, interest is increasing in the problem area of projecting laser beams and imaging over longer, and possibly horizontal paths, where both phase and amplitude effects will corrupt the propagating wave front at the receiver or target. Amplitude errors in a wave front which has passed through a turbulent region are referred to as scintillation. Scintillation arises in optical propagation when turbulence-induced phase aberrations in one region are converted by propagation over long distances to amplitude fluctuations at the receiver or target for the system [2]. Examples of systems whose performance is degraded by scintillation include laser weapon systems and laser communication systems. In the case of laser weapons, turbulence-induced scintillation causes amplitude fluctuations at the target which reduce the energy density that can be applied at the desired point. Turbulence induced scintillation degrades the performance of laser communications systems by causing signal dropouts which reduce the signal-to-noise ratio [1].

The amplitude of an optical wave front can be directly controlled using absorbing elements such as a liquid crystal TV [6]. Unfortunately, absorbing elements are inefficient in their use of light, and are inappropriate for high power laser applications because the power densities involved would destroy any absorbing element. Hence, it is highly desirable to accomplish amplitude control using entirely reflective elements if possible.

Reflective deformable mirrors such as those used in adaptive optics are candidate devices for amplitude control.

An approach to correcting scintillation effects for laser beam projection and imaging systems using two deformable mirrors was published in Ref. [7], which is an extension of the basic concept published by Kanev and Lukin in Refs. [8, 9, 10]. A uniform amplitude beam is assumed to fall on the first deformable mirror. The location of the second deformable mirror is chosen to lie in the far field of the first deformable mirror, and the propagation to the far field is accomplished by use of a Fourier transforming mirror. The problem of determining the phase adjustment to apply to the first deformable mirror is not linear, and cannot be solved in closed form [11, 12]. However, because the fields falling on the first and second deformable mirrors form a Fourier transform pair, the phase of the first deformable mirror can be obtained using an approach based on the Fienup phase retrieval algorithm [13]. The second deformable mirror is used to correct the phase of the beam to achieve field conjugation in the beam transmitted from the aperture. This mirror configuration choice enables the implementation of the phase retrieval based algorithm for determining the phase of the first deformable mirror which is described and evaluated here. Because the phase retrieval algorithm returns the principal value phase for the first deformable mirror, phase unwrapping is implemented using a branch point reconstruction algorithm [14].

The results published in Ref. [7] indicate that in principle the two deformable mirror scintillation compensation technique can, on average, improve the far field diffraction pattern of a beam passed through extended path turbulence, where the goal is to maximize the energy deposited in a small region in beacon plane. However, the study presented in Ref. [7] assumed pointwise control of the deformable mirrors. This assumption is an idealization equivalent to assuming that the deformable mirrors have infinite degrees of freedom. During the course of this project we explored the effects of a realistic segmented deformable mirror model. A simulation of propagation through an extended, horizonatal, constant C_n^2 atmospheric path was used to evaluate the effectiveness of this technique. Two compensation techniques were implemented to correct an outgoing laser beam: (1) conventional phase-only correction based on branch point reconstruction of the beacon field; and (2) field conjugation implemented by the two deformable mirror technique implemented

3

with segmented deformable mirrors. Since the focus of this study is on the effects of realistic deformable mirrors, an idealized wave front sensor is assumed which can measure the amplitude of the incident beacon field and local phase differences on the spatial sampling scale of the simulation. The results of our study indicate that a single deformable mirror controlled with a branch point reconstruction-based approach provides equal or superior performance compared to the two deformable mirror technique.

As a consequence of this finding we began investigating theoretical avenues to process all of the intensity measurements available in an adaptive optical system to obtain the deformable mirror commands. To understand the motivation for this algorithm, a short review of the basic theory of complex-valued variables is presented, and the implications adaptive optical systems operating in the presence of turbulence are discussed. Let the turbulence-corrupted complex optical field in some plane be represented by $U(\mathbf{x})$, and adopt the standard definition of the principal value phase $\psi(\mathbf{x})$ as

$$\psi(\mathbf{x}) = \tan^{-1}\left(\frac{\Im\{U(\mathbf{x})\}}{\Re\{U(\mathbf{x})\}}\right), \tag{1}$$

where $\Re\{U(\mathbf{x})\}$ and $\Im\{U(\mathbf{x})\}$ represent the real and imaginary parts of the complex field, respectively, and $\mathbf{x}$ represents a spatial location in the plane of interest. Inspection of Eq. (1) shows that the principal value phase is defined only on the interval $(-\pi, \pi)$. Hence, in an optical field which has propagated through a turbulent region of the atmosphere a continuous principal value phase function does not in general exist [15, 16]. There are two sources of discontinuities in the principal value phase: (1) so-called "phase wraps", which arise from the phasor representing $U(\mathbf{x})$ moving from the second to the third quadrant of the complex plane, or conversely; and (2) so-called "branch points", which arise from the presence of zeros in the complex field. When plotted, the principal value phase of complex fields which have no branch points may appear discontinuous due to phase wraps, but in fact a continuous phase map with values that lie outside the range of $(-\pi, \pi)$ can be constructed by "unwrapping" the principal value phase [14]. A number of techniques exist to accomplish this unwrapping, or reconstruction process. These techniques are based on computing the discrete gradient of the principal value phase, which corresponds to computing finite phase differences on a

4

sampled grid [3, 16], and the applying either recursive reconstruction, such as used in reconstructing the phase of the Fourier transform of the image in the Knox-Thompson technique of speckle imaging method [3], least squares, minimum variance, or maximum likelihood techniques for fitting smooth elementary functions to the phase differences [3], or by computing the discrete Laplacian of the principal value phase and formulating a solution based on a discrete Poisson's equation solution [14].

The least squares reconstruction paradigm is the most widely used in adaptive optical systems [3, 16]. However, implicit in the derivation of the least squares reconstructor is the assumption that there exists a continuous phase. As discussed in Refs. [15],[14], and [16], when there are branch points in the complex field, a continuous phase does not exist. The presence of branch points is necessarily associated with amplitude fluctuations, or scintillation, in the optical field. Scintillation strength is typically characterized by the variance of the logarithm of the ratio of the actual amplitude at a point to the amplitude of the field resulting from free space propagation from the same source, denoted by σ_χ^2. Theoretical expressions for σ_χ^2 have been developed using a weak fluctuation theory [17, 18], and theoretically obtained values for σ_χ^2 are often referred to as the "Rytov variance", which we will denote by $\sigma_{\chi,R}^2$ to distinguish the theoretical value for the variance of the log amplitude fluctuations from the experimentally observed value. Under conditions where scintillation is negligible $\sigma_{\chi,R}^2$ is small, typically on the order of $\sigma_{\chi,R}^2 \leq 0.05$, and σ_χ^2 and $\sigma_{\chi,R}^2$ are typically in close agreement. As the path length L or the strength of the turbulence C_n^2 increases, $\sigma_{\chi,R}^2$ increases steadily. However, it has been observed experimentally [17] and in simulations [19, 20] that while $\sigma_{\chi,R}^2$ increases steadily as C_n^2 or L increase, the observed fluctuations in the log amplitude σ_χ^2 saturate at a level of $\sigma_\chi^2 \approx 0.3$ [17]. Under conditions of $\sigma_{\chi,R}^2 > 0.05$ branch points generally appear in the turbulence corrupted optical field. As interest grows in using adaptive optical systems to image and propagate laser beams over long paths or through strong turbulence, understanding the opportunities for improving adaptive optical system performance by use of appropriate wave front reconstructors is increasingly important.

A new class of wave front reconstruction algorithms have been developed in the synthetic aperture radar signal processing community which can sense the presence of branch points in high resolution and high signal-to-noise ratio phase difference data, and provide reconstructed phase maps which account for the

5

branch points and associated branch cuts [14]. One branch point reconstruction technique, referred to as Goldstein's algorithm, was implemented and used to study the value of branch point reconstruction in laser beam projection systems. Goldstein's algorithm uses a two step process to reconstruct a wave front: (1) it first locates branch points in the wave front; and (2) it implements a path-dependent phase reconstruction similar to conventional recursive reconstructors [3], with the distinction that phase discontinuities arising from branch points are accounted for in the reconstruction. When branch points are present in the wave front, Goldstein's algorithm computes a discontinuous phase function which when "rewrapped" exactly matches the input wrapped phase in the absence of noise. Unfortunately, a significant practical barrier to implementing Goldstein's algorithm is the need to explicitly find the branch points in realistic wave front sensor data which is spatially averaged and corrupted with measurement noise. These problems may prevent implementing branch point reconstructors with real wave front sensor data, and provide motivation for the study of a nonlinear approach for obtaining deformable mirror commands.

In this report we describe an algorithm for wave front reconstruction and deformable mirror control which attempts to provide performance which is nearly equivalent to branch point reconstructors working with pointwise phase difference data, but does not require that the branch points be located. Rather, the algorithm is based on the premise that information about the phase of the beacon field is encoded in the intensity of the beacon field, the wave front sensor intensity image, and a conventional image formed with light from the beacon. The algorithm developed here is an extension of the algorithm presented in Ref. [21], where it was shown that Hartmann sensor and conventional images could be jointly processed to increase the dynamic range of a Hartmann sensor. An optimal set of weights for wave front reconstruction basis functions or deformable mirror influence functions can be obtained by finding the set of weights which is maximally consistent with a measured Hartmann sensor image and a measured conventional image when the pupil intensity is available to the algorithm. Three measurements are required for this algorithm: (1) the Hartmann sensor image; (2) a conventional image formed with light from the beacon field; and (3) a beacon intensity map. The phase of the incident field is estimated by a linear combination of influence functions in a nonlinear optimization-based algorithm. For comparison purposes we have also implemented

6

idealized least squares and a branch point reconstructor based on Goldstein's algorithm, both of which use the output of an idealized pointwise phase difference sensor, and a conventional least squares reconstructor based on centroid processing of Hartmann sensor output. We have found that the algorithm developed here provides significantly improved performance over a conventional least squares Hartmann sensor processing algorithm under conditions of strong and saturated scintillation, and with performance almost equivalent to Goldstein's algorithm in a laser beam projection paradigm with finite degree-of-freedom, phase-only adaptive optics implemented in the transmitter. One benefit of the algorithm presented here is that the need for point-by-point phase differences required by Goldstein's algorithm is eliminated, making this algorithm attractive for systems which must operate in the presence of scintillation.

The remainder of this report is organized as follows. The theoretical basis and supporting analysis are presented in Section 2. The simulation used to evaluate performance is discussed in Section 3. Theoretical and simulation results are presented in Section 4, and experimental results are presented in Section 5. Conclusions are drawn in Section 6.

2 Technical analysis.

In this section the theoretical analysis of the scintillation compensation concept is presented. This section begins with the basic phase-retrieval based approach to the laser beam projection problem which assumes the ability to control an optical wave front with a very high degree of freedom deformable mirror. Since deformable mirrors with such a large number of degrees of freedom are currently an idealization, scintillation control with modal mirrors was then investigated. Use of modal mirrors requires a significantly different approach to determining the deformable mirror commands since such mirrors cannot be controlled on a "point-wise" basis as was assumed for the early work. The approach for determining the modal mirror commands is based on nonlinear optimization. This section concludes with the development of the nonlinear optimization theory for using modal mirrors. The scintillation control studies implemented for imaging follow directly from the laser beam projection work, and as a consequence, a less detailed theoretical treatment is

presented for the imaging work.

The functional block diagram for the scintillation correction system for laser beam projection is shown in Fig. 1. It is assumed that a beacon wave front is available from the object which carries the amplitude and phase corruption induced by propagation from the object to the telescope, and hence carries information about the beacon field. The mechanism by which this beacon is provided is not treated here, though we note that obtaining a suitable beacon is a serious issue affecting the practical implementation of this technique. The intensity and phase of the incident beacon wave front is measured with a suitable device, such as a Hartmann sensor, which is sensitive to both the local gradient of the phase and the intensity of the incident wave front [3]. The wave front sensor outputs are processed to compute the amplitude and the phase of the field in the telescope aperture. Phase retrieval routines process the beacon amplitude and phase measurements to determine the phase deformation to apply to the deformable mirrors DM_1 and DM_2 to conjugate the field due to the beacon. It is assumed that a collimated laser beam is incident on DM_1. The deformable mirror computer contains the phase retrieval algorithm which computes the phase distortion to apply to DM_1. The goal is to apply a phase distortion to DM_1 which provides a close match to the desired amplitude distribution when the light falls on DM_2. DM_2 lies in the Fraunhofer diffraction region of DM_1 due to use of the Fourier transforming mirror shown in Fig. 1, and DM_2 is assumed to be optically conjugate to the pupil plane of the beam projection system. The purpose of DM_2 is to correct the phase distribution of the outgoing beam so that the field is approximately conjugated to the incident field from the beacon as it leaves the aperture. Two approaches for controlling DM_1 are now discussed: pointwise control of DM_1, and modal control of DM_1.

2.1 Pointwise control of DM_1.

Let the complex-valued wave front incident on the aperture from the beacon $\tilde{U}_b(\vec{x}_f)$ be represented by

$$\tilde{U}_b(\vec{x}_f) = A_b(\vec{x}_f) \exp\left\{ j\psi_b(\vec{x}_f) \right\},\tag{2}$$
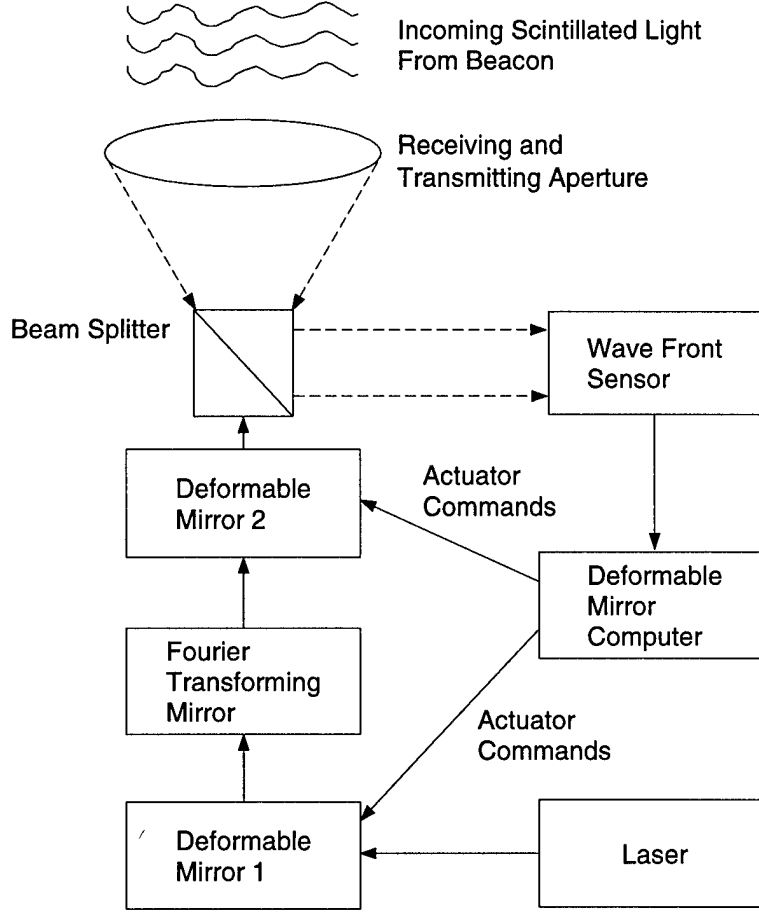
Figure 1: Block diagram for scintillation correction system.

where $\vec{x}_f$ is a position vector in the telescope pupil, $A_b(\vec{x}_f)$ is the amplitude of the beacon field, $\psi_b(\vec{x}_f)$ is the phase of the beacon field, and the tilde is used to indicate a complex-valued function. Let the amplitude and phase of the beam transmitted by the aperture $\tilde{U}_t(\vec{x}_f)$ be represented by

$$\tilde{U}_t(\vec{x}_f) = B(\vec{x}_f) \exp\left\{j\psi_t(\vec{x}_f)\right\}, \tag{3}$$

where $B(\vec{x}_f)$ represents the amplitude of the field reflected from DM_2, and $\psi_t(\vec{x}_f)$ represents the phase of the field reflected from DM_2. In the laser beam projection context, optical field conjugation means that

$B(\vec{x}_f)$ and $\psi_t(\vec{x}_f)$ are adjusted so that [22]

$$B(\vec{x}_f) \propto A_b(\vec{x}_f), \tag{4}$$

and

$$\psi_t(\vec{x}_f) = -\psi_b(\vec{x}_f), \tag{5}$$

where the notation $z_1 \propto z_2$ is used to represent the "proportional to" relational concept. Note that in writing Eq. (4) we have assumed that the amplitude of $B(\vec{x}_f)$ is small enough so that there are no nonlinear effects such as blooming [8, 23]

The amplitude of the field illuminating DM_2 is established by applying a phase deformation to DM_1, and projecting the resulting field into the Fraunhofer diffraction region using the Fourier transforming mirror [24]. The field falling on DM_1 is assumed to be a well-collimated laser beam of amplitude A. The field leaving DM_1 $\tilde{U}_1(\vec{x})$ has amplitude A and a phase profile imparted by DM_1

$$\tilde{U}_1(\vec{x}) = A \exp\{j\psi_1(\vec{x})\}. \tag{6}$$

Letting the field illuminating DM_2 be represented by $\tilde{U}_2(\vec{x}_f)$, we obtain

$$\tilde{U}_2(\vec{x}_f) = FT\left[\tilde{U}_1(\vec{x})\right] = B(\vec{x}_f) \exp\{j\phi(\vec{x}_f)\}, \tag{7}$$

where $\vec{x}$ is a spatial coordinate in the plane of DM_1, $FT\left[\cdot\right]$ represents the Fourier transformation operator, $\vec{x}_f = \vec{f}\lambda f_l$ where $\vec{f}$ is the independent spatial frequency variable which arises from the Fourier transform operation of Eq. (7) and f_l is the focal length of the Fourier transforming mirror, $\psi_1(\vec{x})$ represents the phase distortion applied to DM_1, and $\phi(\vec{x}_f)$ represents the phase of the wave front falling on DM_2. The purpose of DM_2 is to apply a phase distortion to $\tilde{U}_2(\vec{x}_f)$ such that the complex transmitted field has phase equal to $-\psi_b(\vec{x})$.

The relationship between the phase $\psi_1(\vec{x})$ applied to DM_1 and the amplitude $B(\vec{x}_f)$ which is incident on DM_2 is not linear, and no squared error metric can be defined which would yield a term linear in $\psi_1(\vec{x})$ when differentiated with respect to $\psi_1(\vec{x})$. Hence, an iterative approach to determining the optimal $\psi_1(\vec{x})$ is adopted here which is based on the phase retrieval algorithm [12, 13]. A functional block diagram of the algorithm used here is shown in Fig. 2.

The starting point for the algorithm is shown in the upper left-hand corner of Fig. 2. A plane wave of amplitude A, which physically corresponds to the amplitude of a well-collimated laser beam falling on DM_1, is associated with a random guess for $\psi_1(\vec{x})$, the phase of DM_1. The field leaving DM_1, $A \exp\{j\psi_1(\vec{x})\}$, is then projected into its Fraunhofer diffraction region by use of a fast Fourier transform (FFT), which physically corresponds to the function performed by the Fourier transforming mirror shown in Fig. 1. The outcome of this step is represented by $B(\vec{x}_f) \exp\{j\phi(\vec{x}_f)\}$, and physically corresponds to the field which would fall on DM_2 due to the particular $\psi_1(\vec{x})$. The Fourier domain constraint that the field falling on DM_2 should satisfy Eq. (4) is enforced by substituting the desired field amplitude $B'(\vec{x}_f)$ for $B(\vec{x}_f)$, where $B'(\vec{x}_f)$ is given by

$$(B'(\vec{x}_f))_{\text{norm}} = (A_b(\vec{x}_f))_{\text{norm}} . \tag{8}$$

The subscript "norm" in Eq. (8) is used to indicate that the terms on both sides of the equality symbol have been normalized to have unit energy. The quantity $B'(\vec{x}_f) \exp\{j\phi(\vec{x}_f)\}$ is then projected back into the plane of DM_1 by use of an inverse FFT to obtain $A'(\vec{x}) \exp\{j\psi_1(\vec{x})\}$, where the $\psi_1(\vec{x})$ term is taken to be the "next" step in determining the ultimate figure of DM_1. The uniform field amplitude A is then substituted for $A'(\vec{x})$, returning the algorithm to the upper left-hand corner of Fig. 2. This process is repeated until the stopping criterion is satisfied.

The stopping criterion used here is based on the convergence of a measure of the squared error σ^2 between the normalized amplitude of the field falling on DM_2, $(B(\vec{x}_f))_{\text{norm}}$, and the normalized beacon
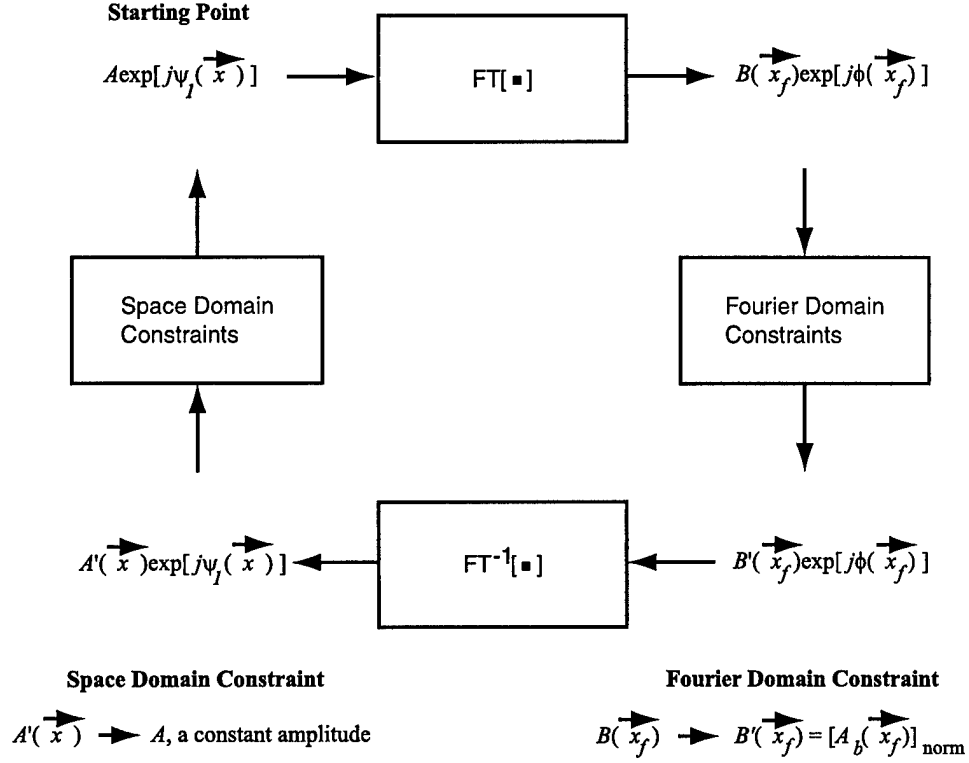
Starting Point

$A\exp[j\psi_I(\vec{x})]$ $\longrightarrow$ FT[$\bullet$] $\longrightarrow$ $B(\vec{x}_f)\exp[j\phi(\vec{x}_f)]$

Space Domain Constraints

Fourier Domain Constraints

$A'(\vec{x})\exp[j\psi_I(\vec{x})]$ $\longleftarrow$ FT^{-1}[$\bullet$] $\longleftarrow$ $B'(\vec{x}_f)\exp[j\phi(\vec{x}_f)]$

Space Domain Constraint

$A'(\vec{x})$ $\longrightarrow$ A, a constant amplitude

Fourier Domain Constraint

$B(\vec{x}_f)$ $\longrightarrow$ $B'(\vec{x}_f) = [A_b(\vec{x}_f)]_{\text{norm}}$

Figure 2: Block diagram of phase retrieval technique used for controlling the amplitude of the field falling on DM_2.

field amplitude $(A_b(\vec{x}_f))_{\text{norm}}$ given by

$$\sigma^2 = \int \left[\left| (A_b(\vec{x}_f))_{\text{norm}} \right| - \left| (B(\vec{x}_f))_{\text{norm}} \right| \right]^2 d\vec{x}_f. \tag{9}$$

Letting $\sigma(k)$ represent the value of σ obtained in the kth iteration, the stopping criterion is that the kth $\psi_1(\vec{x})$ is taken as the final figure of DM_1 when the condition

$$\frac{|\sigma(k) - \sigma(k-1)|}{\sigma(k-1)} \leq 10^{-4} \tag{10}$$

is satisfied. We note that this stopping criterion does not guarantee that a global minimum error has been found. Rather, this stopping criterion indicates that $\psi_1(\vec{x})$ has stopped changing from iteration to iteration.

2.2 Modal control of DM_1 and DM_2.

The derivation presented in Section 2.1 assumes that the phase of a wave front can be controlled on a pointwise basis. This level of control is an idealization which cannot now be realized in practice. The phase retrieval algorithm provides the principal value, or "wrapped" phase $\psi_1(\vec{x})$ due to the use of Fourier transforms in the calculation. The wrapped phase contains discontinuities due to the complex phasor representation of $\exp\{\psi_1(\vec{x})\}$ moving from the second to the third quadrant of the complex plane, and because the full field propagated backwards from the DM_2 plane to the DM_1 plane after the constraints are imposed in general contains branch points. Because of these discontinuities, fitting a deformable mirror directly to the $\psi_1(\vec{x})$ which is output by the phase retrieval algorithm will have large fitting errors. To reduce the fitting error we have implemented a branch point reconstruction algorithm known as Goldstein's algorithm [14] which we use to "unwrap" $\psi_1(\vec{x})$. We denote the unwrapped phase by $\psi_1^U(\vec{x})$. The unwrapped phase $\psi_1^U(\vec{x})$ will still contain discontinuities, but we have found that effects due to fitting error are much smaller when phase unwrapping is implemented.

The segmented mirror was specified by the center-to-center spacing of the square actuators, and it was assumed that there was no dead space between actuators. In the simulation there were never fewer than 3×3 pixels used to model individual actuators. The positions of the individual actuators was determined by assigning the actuator to have the same value as $\psi_1^U(\vec{x})$ at the location of the center location of the actuator. Since the segmented mirror actuators do not spatially overlap the individual influence functions are orthogonal, and hence, no additional processing is required to determine the figure for DM_1.

The field falling on DM_1 was modeled as being a uniform amplitude plane wave, such as might be obtained from a well-collimated laser beam with amplitude A. The field falling on DM_2, denoted in by $\tilde{U}_2(\vec{x}_f)$, was calculated using Eq. (7), using an FFT to accomplish the Fourier transform operation. The phase of DM_2, denoted by $\psi_2(\vec{x}_f)$, must compensate both for the phase of the field arriving from DM_1, represented by $\phi(\vec{x}_f)$ in Eq. (7), and for the phase of the atmosphere $\psi_b(\vec{x}_f)$, so that in principle

$$\psi_2(\vec{x}_f) + \phi(\vec{x}_f) = -\psi_b(\vec{x}_f). \tag{11}$$

13

In practice, we have found that the field falling on DM_2 also contains branch points, and hence it is necessary to unwrap the phase which we wish to apply to DM_2. The unwrapped phase for DM_2 $\psi_2^U(\vec{x}_f)$ was found by providing the wrapped phase given by $\arg\{\exp\{-\phi(\vec{x}_f)\}\exp\{-\psi_b(\vec{x}_f)\}\}$ to Goldstein's algorithm. A segmented deformable mirror was also fit to $\psi_2^U(\vec{x}_f)$ to obtain the actual figure for DM_2 $\psi_2(\vec{x}_f)$. The outging field was calculated by computing

$$\tilde{U}_t(\vec{x}_f) = \tilde{U}_2(\vec{x}_f)\exp\{\psi_2(\vec{x}_f)\}. \tag{12}$$

2.3 A new algorithm for controlling a single deformable mirror.

We consider wave front reconstruction in the context of a horizontal path adaptive optical laser beam projection system. The basic geometry is shown in Fig. 3. We have modeled propagation through a three dimensional volume of turbulence by using a layered model for the atmosphere [3, 19]. A point source beacon illuminates the turbulence volume, and the turbulence-corrupted beacon field is intercepted by the aperture. An ideal lens is placed in the aperture of the system and has focal length equal to the path length so that an outgoing plane wave would be focused at the beacon location in the absence of turbulence. We shall refer to the complex field emanating from the beacon that is intercepted by the telescope pupil as the beacon field, and denote it by $U_B(\mathbf{x}_P) = A_B(\mathbf{x}_P)\exp\{j\psi_B(\mathbf{x}_P)\}$, with intensity $I_B(\mathbf{x}_P) = |U_B(\mathbf{x}_P)|^2$, where $\mathbf{x}_P$ is a two dimensional coordinate in the pupil plane. A single deformable mirror and a Hartmann wave front sensor are placed optically conjugate to the receiver aperture. In addition to the Hartmann sensor measurement, it is assumed that the intensity of the beacon field in the receiver plane can be measured, and that a conventional image is also formed with the beacon field. The outgoing beam initially has uniform intensity, and it is focused so that in the absence of turbulence an Airy disk would be present at the beacon location. The phase of the outgoing beam is modified using a simulated deformable mirror whose figure is adjusted by four techniques to perform compensation on the outgoing beam: (1) a conventional Hartmann sensor centroid-based least squares reconstruction algorithm [3]; (2) a branch point reconstructor known as Goldstein's algorithm [14] which requires as input idealized (and in practice unobtainable) pointwise phase differences; (3) a least
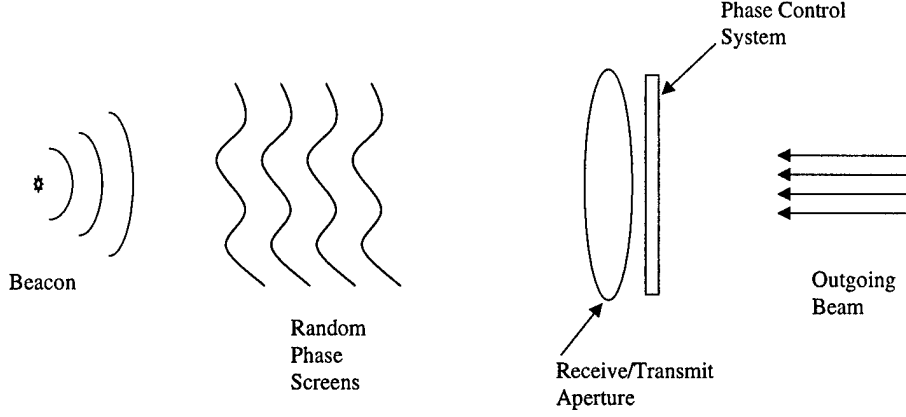
14

Figure 3: Geometry for laser beam projection system.

squares reconstructor which also requires as input idealized (and in practice unobtainable) pointwise phase differences; and (4) the new nonlinear optimization-based algorithm described here. It should be noted that the branch point and idealized least squares reconstructions would not be obtainable in practice, but are computed to serve as comparative measures of performance. For example, the performance of the idealized branch point reconstructor serves as an upper bound on the performance of the nonlinear optimization-based technique developed here, and the idealized least squares reconstructor serves as an upper bound on the performance of the Hartmann sensor-based least squares reconstruction. The compensated beam is propagated back through the turbulent volume to the beacon plane, where statistical quantities of interest are accumulated to evaluate the performance of the various compensation approaches.

Since we are interested in studying the effects of scintillation on wave front sensing in extended path turbulence we have modeled a 100 km path using 10 equally spaced turbulent layers, with the first layer 10 km from the beacon, and the final layer lying in the aperture. The ten layer model is justified in this case by the close match between the Rytov variance computed for spherical wave propagation through a region of constant C_n^2 given by [17]

$$\sigma_{\chi,R}^2 = 0.56 k^{7/6} \int_0^L \mathrm{d}z C_n^2(z) \left(\frac{z}{L}\right)^{5/6} (L-z)^{5/6}, \tag{13}$$

15

and the Rytov variance calculated by assuming the turbulence lies in layers given by

$$\sigma^2_{\chi,\text{layer}} = 0.56 k^{7/6} \Delta_L C_n^2 \sum_{n=1}^{10} \left(\frac{n\Delta_L}{L} \right) (L - n\Delta_L)^{5/6}, \tag{14}$$

where $\Delta_L = 10$ km is the layer thickness. For example, when $C_n^2 = 1 \times 10^{-18}$ $\sigma^2_{\chi,R} = 0.158$, while $\sigma^2_{\chi,\text{layer}} = 0.155$.

The phase of an arbitrary random screen is denoted by $\psi_R(\mathbf{x})$, where $\mathbf{x}$ is a coordinate in the random screen plane, so that the field immediately after a random screen has the form

$$U_R(\mathbf{x}) = U_A(\mathbf{x}) \exp\{j\psi_R(\mathbf{x})\}, \tag{15}$$

where $U_A(\mathbf{x})$ is the field incident on the random screen. For each screen the field $U_R(\mathbf{x})$ lies in the Fresnel region of the next screen or, in the case of the last screen, in the receive/transmit aperture [24]. An angular spectrum propagator was used to perform the near field propagations [7]. The beacon field is passed through a simulated lens which would be perfectly focused on the beacon in the absence of turbulence, and thus having complex transmittance given by

$$t_l(\mathbf{x}_P) = \exp\left\{ -j\frac{k}{2L}(|\mathbf{x}_P|^2) \right\} \tag{16}$$

where the total path length $L = 100$ km, and $\mathbf{x}_P$ is a two dimensional coordinate in the pupil plane. Phase only corrections of an outgoing, initially planar beam are calculated in the aperture plane, and the corrected beam is passed through the lens and propagated in reverse through the phase screens to the beacon plane. In the beacon plane the intensity distribution of the various correction schemes is calculated, and statistical quantities needed to compute the mean and the variance of the intensity distribution are accumulated. These intensity statistics form the basis for comparing the least squares and branch point correction schemes investigated here.

We have implemented a principal phase difference-sensitive wave front sensor with resolution equal to the

sample spacing in the simulation to provide idealized wave front sensor input into the idealized branch point and least squares reconstructors. The wave front sensor measures principal value phase differences (or some quantity proportional to the principal value phase differences) on a sampled grid in $\mathbf{x}_P$-space denoted by the discrete integer coordinates (i,j), with $0 \le i \le M-1$ and $0 \le j \le N-1$. Horizontal phase differences $\Delta^x(i,j)$ and vertical phase differences $\Delta^y(i,j)$ are assumed to be known modulo 2π on a discrete grid with locations designated by (i,j). The phase differences are defined by [14]

$$\Delta^x(i,j) = \arg\left[\exp\{j\left(\psi_B(i+1,j) - \psi_B(i,j)\right)\}\right], \tag{17}$$

and

$$\Delta^y(i,j) = \arg\left[\exp\{j\left(\psi_B(i,j+1) - \psi_B(i,j)\right)\}\right], \tag{18}$$

where $\arg[\cdot]$ is an operator which takes the phase of a complex-valued quantity. As can be seen by Eqs. (17) and (18), the phase differences obtained in this fashion are the principal value phase differences which are the typical output of wave front sensors used in adaptive optical systems [16]. Branch points in the field $U_B(\mathbf{x})$ will rarely (if ever) fall directly on a sample point [16, 14], and hence, searching for a zero in the incident field is a poor strategy for locating branch points. Rather, the phase differences are summed around all possible 2×2 collections of samples using

$$\Sigma(i,j) = -\Delta^x(i,j) - \Delta^y(i+1,j) + \Delta^x(i,j+1) + \Delta^y(i,j). \tag{19}$$

When $\Sigma(i,j) = 0$ no branch point is enclosed, and no phase discontinuity exists at (i,j). However, when $\Sigma(i,j) = \pm 2\pi$, a branch point is enclosed by the loop, and it is expected that a discontinuity in the reconstructed phase will originate at this point. The location and "polarity", or sign of the 2π term are noted and used in branch point reconstruction algorithms. The branch point reconstruction algorithm used in this paper is generally referred to as the Goldstein algorithm (though the seminal paper is by Goldstein, Zebker and Werner), which has been fully discussed elsewhere [14]. Here we confine ourselves to qualitatively

17

summarizing the algorithm and providing an example of its performance. Wrapped phase differences are input to Goldstein's algorithm. Branch points are located as described in the discussion of Eq. (19), and their polarity is noted. A heuristic approach based on the region growing concept of image processing [25] is used to connect the nearest pairs of positive and negative branch points. Branch cuts are constructed along the paths defined by pairs of positive and negative branch points. A phase reconstruction approach similar to the recursive algorithm is then implemented, but with the significant exception that *no path is allowed to encircle a branch point or cross a branch cut.* As a direct consequence, the reconstructed phase is discontinuous at the branch cuts. The unwrapped phase reconstructed with the branch point reconstructor is denoted by $\phi_{\mathrm{BP}}(i,j)$. The Goldstein algorithm is known to provide accurate results except in regions which are completely enclosed by branch cuts. However, in our experience, the Goldstein algorithm has not failed when applied to phase functions created by simulating laser propagation through the atmosphere.

We now present an example of the performance of the Goldstein algorithm. Figure 4(a) shows the wrapped phase $\arg[\exp\{j\psi_B(i,j)\}]$ of an incident beacon field simulated as described in Section 3. This function was input to the Goldstein algorithm, and the unwrapped output $\phi_{\mathrm{BP}}(i,j)$ is shown in Fig. 4(b), where the detected branch points are shown. Figure 4(b) is hard to interpret since the dynamic range of the unwrapped phase is much larger than the dynamic range of the wrapped phase. Hence, in Fig. 4(c) we show the rewrapped phase given by $\arg\left[\exp\{j\phi_{\mathrm{BP}}(i,j)\}\right]$. Detailed comparison of Fig. 4(a) and Fig. 4(c) shows that the Goldstein algorithm provides an exact phase unwrapping in this case to within an insignificant piston term.

Real deformable mirrors have a finite number of degrees of freedom, and as a consequence $\phi_{\mathrm{BP}}(i,j)$ can not in general be fit perfectly with a real deformable mirror. Here we modeled a deformable mirror with influence functions $e_k(\mathbf{x}_P)$ consisting of a collection of two dimensional linear spline functions, also referred to as two dimensional triangle functions, placed on a Cartesian grid with user selected spacing D, represented by [26]

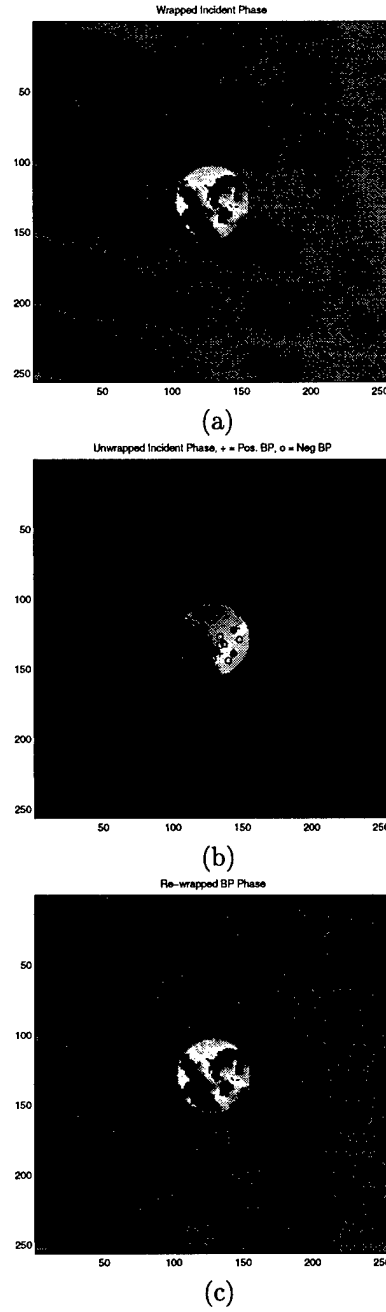$$e_k(\mathbf{x}_P) = \Lambda\left(\frac{\mathbf{x}_P - \mathbf{x}_k}{D}\right), \tag{20}$$

Figure 4: Example of branch point reconstruction by the Goldstein algorithm for a laser beam propagation problem: (a) the wrapped incident phase ψ_I; (b) the unwrapped phase ϕ_I output by the Goldstein algorithm with positive and negative branch points indicated by (+) and (o), respectively; and (c) the rewrapped phase given by $\arg[\exp\{j\phi_I(i,j)\}]$.

19

where $\mathbf{x}_k$ is the center location of the kth actuator projected into pupil space. It should be noted that the bases of linear splines defined this way are $2D$ wide, so that with the arrangement used here the line segments defining where one influence function goes to zero fall directly under the peaks of the adjoining influcence functions. These actuators were fit to $\phi_{\text{BP}}(i,j)$ using a three step process [3]:

1. The reconstructed phase, $\phi_{\text{BP}}(i,j)$ is projected onto the actuators using

$$p_k = \frac{\sum_{i,j} W(i,j)\phi_{\text{BP}}(i,j)e_k(i,j)}{\sum_{i,j} |e_k(i,j)|^2}, \tag{21}$$

where p_k is the projection of $\phi_{\text{BP}}(i,j)$ onto the kth actuator, and $W(i,j)$ is a pupil function defined to be unity inside the pupil, and zero outside the pupil. This calculation is of necessity performed at the resolution of the simulation since the values of $\phi_{\text{BP}}(i,j)$ only exist on the sample grid. The entries of p_k can be arranged into a vector we denote by $\bar{p}$.

2. Since the influence functions are not orthogonal the influence function interaction matrix R must be computed with elements given by [3]

$$r_{kl} = \int d\mathbf{x}_P W(\mathbf{x}_P)e_k(\mathbf{x}_P)e_l(\mathbf{x}_P). \tag{22}$$

In our implementation Eq. (22) is computed with high accuracy using numerical quadrature to provide for a stable inverse of R. The weight vector $\bar{c}$, containing the values of c_k for the influence functions, is then computed from

$$\bar{c} = R^{-1}\bar{p}. \tag{23}$$

3. Finally, the deformable mirror phase fit to $\phi_{\text{BP}}(i,j)$ is reconstructed using

$$\phi_{\text{BP}}^{DM}(i,j) = \sum_k c_k e_k(i,j), \tag{24}$$

where the superscript DM is used to represent the phase of the deformable mirror applied to the

20

outgoing beam.

The basic principle of the idealized least squares wave front reconstruction is straightforward. We assume that the pointwise wave front sensor has as its output a vector of x and y-directed phase differences denoted by $\overline{\Delta\phi}$. Representing the vectorized input phase on a sampled grid using the notation $\overline{\phi}$, we can define the relationship

$$\overline{\Delta\phi} = \mathbf{P}\overline{\phi}, \tag{25}$$

where $\mathbf{P}$ is a matrix containing 1's, -1's, and 0's, and is ordered so that the correct combinations of the elements of $\overline{\phi}$ are used to compute each element of $\overline{\Delta\phi}$ [16, 14]. The least squares estimate of $\overline{\phi}$ is given by

$$\overline{\phi}_{\text{LMSE}} = \left(\mathbf{P^T P}\right)^{-1} \mathbf{P^T} \overline{\Delta\phi}, \tag{26}$$

and the elements of the vector $\overline{\phi}_{\text{LMSE}}$ are rearranged into an array denoted by $\phi_{\text{LMSE}}(i,j)$. The deformable mirror is then fit to $\phi_{\text{LMSE}}(i,j)$ using the process described in Eqs. (21) to (24) to obtain the deformable mirror figure associated with the idealized least squares reconstruction $\phi^{DM}_{\text{LMSE}}(i,j)$. In principle, least squares phase reconstruction based on Eq. (26) is quite simple, but in practice sparse matrix techniques may be required to implement Eq. (26). When phase differences computed from a continuous input phase are used in this algorithm in the absence of noise the output phase $\phi_{\text{LMSE}}(i,j)$ matches the input phase to within an insignificant piston term [16].

Due to the use of pointwise phase difference data the deformable mirror phase $\phi^{DM}_{\text{BP}}(i,j)$ and $\phi^{DM}_{\text{LMSE}}(i,j)$ are idealizations that can not be obtained experimentally. Rather, Hartmann sensor, or other wave front sensor data is generally used to obtain deformable mirror commands using a least squares fitting criterion. A Hartmann sensor consists of an array of lenslets placed one focal length in front of a camera, as shown in Fig. 5 [3]. Light falling on an individual lenslet is focused to a spot in the focal plane which is in general is displaced from the optical axis of the lenslet due to turbulence effects. The centroid of the intensity distribution of the light in the detector plane can be calculated for each lenslet, and the local slope of the

21

wave front can be calculated using

$$\mathbf{s} = k\frac{\mathbf{x}_c}{f_l} \tag{27}$$

where $\mathbf{x}_c$ is the two dimensional centroid location, and f_l is the focal length of the lenslet. The least squares criterion minimizes the sum square of the error between the measured slopes, and the slopes which would arise from a linear combination of actuator influence functions. This minimization is accomplished by defining the error

$$\Delta = \bar{s} - H\bar{c} \tag{28}$$

where $\bar{s}$ is a vector containing the measured slopes from all of the subaperture, $\bar{c}$ is a vector containing all of the deformable mirror weights, and H is a Jacobian matrix with the entry in the mth row and q^{th} column given by

$$H_{m,q} = \frac{\partial s_m}{\partial c_q}. \tag{29}$$

Minimizing the squared error defined by $\Delta^T\Delta$ yields the least squares set of actuator commands [3]

$$\bar{c}^{LSH} = \left(H^T H\right)^{-1} H^T \bar{s}. \tag{30}$$

The least squares estimate for the deformable mirror figure is obtained by substituting the values of $\bar{c}^{LS}$ into Eq. (24) to obtain deformable mirror figure obtained from the Hartmann sensor data $\phi^{DM}_{\text{LSH}}(i,j)$.

The new algorithm is an extension of the algorithm presented in Ref. [21], where it was shown that the entire Hartmann sensor image and a conventional image could be jointly processed to increase the dynamic range of the Hartmann sensor. This algorithm uses a parameterized form for the deformable mirror figure given by Eq. (24), but with a different approach to calculating the weights c_k. We seek to estimate $\bar{c}$ from measurements of the wave front sensor image intensity $I_W(\mathbf{x}_W)$, where $\mathbf{x}_W$ is a two dimensional coordinate in the Hartmann sensor image plane, the pupil plane intensity $I_P(\mathbf{x}_P)$, and the conventional image plane intensity $I_C(\mathbf{x}_C)$, where $\mathbf{x}_C$ is a two dimensional coordinate in the conventional image plane. The optimization is accomplished by forming an objective function $J(\bar{c})$, and minimizing $J(\bar{c})$ by the choice
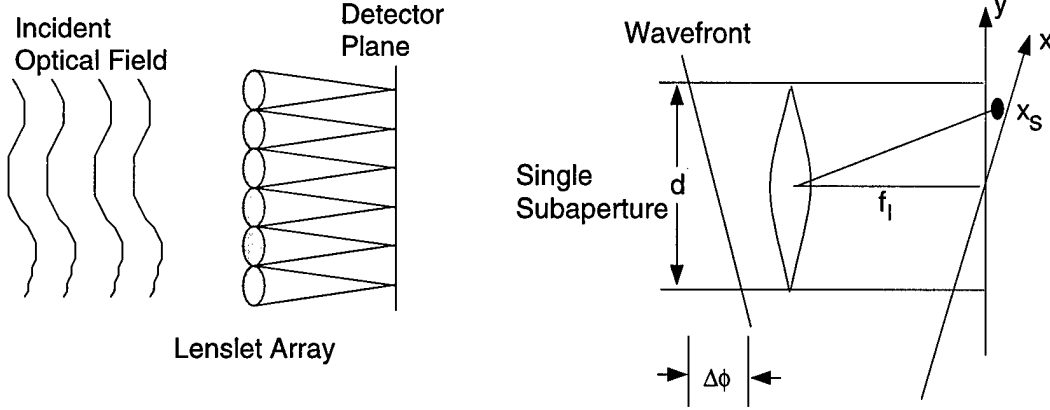
Figure 5: Diagram of the Hartmann wave front sensor.

of $\bar{c}$. The objective function used here is given by

$$J(\bar{c}) = \sum_{\mathbf{x}_W} \left[(I_W(\mathbf{x}_W))^{1/2} - \left(\tilde{I}_W(\mathbf{x}_W, \bar{c}) \right)^{1/2} \right]^2 + \sum_{\mathbf{x}_C} \left[(I_C(\mathbf{x}_C))^{1/2} - \left(\tilde{I}_C(\mathbf{x}_C, \bar{c}) \right)^{1/2} \right]^2, \qquad (31)$$

where $\tilde{I}_W(\mathbf{x}_W, \bar{c})$ and $\tilde{I}_C(\mathbf{x}_C, \bar{c})$ represent the wave front sensor and conventional images computed from the current guess of the vector $\bar{c}$, respectively. The objective function in Eq. (31) is an extension of one of the objective functions used in phase retrieval [27]. Also, the availability of the beacon field intensity information $I_B(\mathbf{x}_P)$ provides a significant extension to the approach used in [21] due to the fact that $[I_B(\mathbf{x}_P)]^{1/2} = |U_B(\mathbf{x}_P)|$ can be used in computing $\tilde{I}_W(\mathbf{x}_W, \bar{c})$ and $\tilde{I}_C(\mathbf{x}_I, \bar{c})$ as described below. The objective function in Eq. (31) can be minimized using quasi-Newton methods [28, 29], either with or without the use of an analytic gradient vector $\overline{\nabla J}$, with k^{th} element given by

$$\nabla_k J = \frac{\partial J(\bar{c})}{\partial c_k}. \qquad (32)$$

If no analytic gradient is used, then it is necessary to perturb each parameter c_k at each step to evaluate

both $\overline{\nabla J}$ and the Hessian matrix $\mathbf{H}$ of $J(\overline{\alpha})$ with $(k,l)^{\text{th}}$ element given by

$$H_{kl} = \frac{\partial^2 J(\overline{c})}{\partial c_k \partial c_l}.$$

(33)

This perturbation-based approach to estimating $\overline{\nabla J}$ and $\mathbf{H}$ is computationally expensive. Hence, an analytic gradient $\overline{\nabla J}$ was calculated. The details of this analysis are described in [21], and we present only the results of the analysis here. Note that the objective function in Eq. (31) has two terms which are summed: one due solely to the wave front sensor image, and one due solely to the conventional image, and we let these two contributions to the objective function be represented by $J_W(\overline{c})$ for the wave front sensor channel, and $J_C(\overline{c})$ for the conventional image channel. The gradients of these two terms are given by

$$
\begin{aligned}
\frac{\partial J_W(\overline{c})}{\partial c_k} &= 2\Im \left\{ \sum_{\mathbf{x}_P} t_H(\mathbf{x}_P) e_k(\mathbf{x}_P) \exp \left\{ j \sum_k c_k e_k(\mathbf{x}_P) \right\} \right. \\
&\quad \times \left. \left[\sum_{\mathbf{x}_W} \left(\frac{I_W(\mathbf{x}_W)}{\tilde{I}_W(\mathbf{x}_W, \overline{c})} \right)^{1/2} \tilde{U}_W^*(\mathbf{x}_W, \overline{c}) h_W(\mathbf{x}_P, \mathbf{x}_W) \right] \right\},
\end{aligned}
$$

(34)

and

$$
\begin{aligned}
\frac{\partial J_C(\overline{c})}{\partial c_k} &= 2\Im \left\{ \sum_{\mathbf{x}_P} P(\mathbf{x}_P) e_k(\mathbf{x}) \exp \left\{ j \sum_k c_k e_k(\mathbf{x}) \right\} \right. \\
&\quad \times \left. \left[\sum_{\mathbf{x}_C} \left(\frac{I_C(\mathbf{x}_C)}{\tilde{I}_C(\mathbf{x}_i, \overline{c})} \right)^{1/2} \tilde{U}_C^*(\mathbf{x}_C, \overline{c}) h_C(\mathbf{x}_P, \mathbf{x}_C) \right] \right\},
\end{aligned}
$$

(35)

where $\mathbf{x}_P$ represents a pupil plane coordinate, $\mathbf{x}_C$ represents a conventional image plane coordinate, and $\mathbf{x}_W$ represents a Hartmann sensor image plane coordinate. In Eq. (34) the term $t_H(\mathbf{x}_P)$ is the complex transmittance of a Hartmann sensor lenslet array with square lenslets of side length d and focal length f_l

$$t_H(\mathbf{x}_P) = \sum_S \exp \left\{ j \frac{k_w}{2 f_l} |\mathbf{x}_P - \mathbf{x}_c(s)|^2 \right\} \text{rect} \left(\frac{\mathbf{x}_P - \mathbf{x}_c(s)}{d} \right),$$

(36)

where $k_w = 2\pi/\lambda$, λ is the mean wavelength of the light, S is the number of subapertures, and $\mathbf{x}_c(s)$ is

the center of the sth subaperture, the term $h_W(\mathbf{x}_P, \mathbf{x}_W)$ is the propagation kernel for propagation from the back of the lenslet array to the lenslet focal plane, $\tilde{U}_W^*(\mathbf{x}_W, \bar{c})$ is the conjugate of the field estimate in the wave front sensor detector plane associated with the current state of $\bar{c}$, and $\tilde{I}_W(\mathbf{x}_W, \bar{c}) = \left|\tilde{U}_W(\vec{x}_W, \bar{c})\right|^2$. The propagation from the back of the Hartmann sensor lenslet array to its detector plane is implemented with an angular spectrum propagator [21, 24], and the field propagated is given by $|U_B(\mathbf{x}_P)| \exp\{\sum_k c_k e_k(i,j)\}$, incorporating information about the amplitude fluctuations of the beacon field into the algorithm. In Eq. (35) the term $P(\mathbf{x}_P)$ represents the physical extent of the pupil, $\tilde{U}_C^*(\mathbf{x}_C, \bar{c})$ is the conjugate of the conventional image field estimate associated with the current state of $\bar{c}$, $\tilde{I}_C(\mathbf{x}_i, \bar{c}) = \left|\tilde{U}_C(\mathbf{x}_C, \bar{c})\right|^2$, and $h_C(\mathbf{x}_P, \mathbf{x}_P)$ is the propagation kernel from the pupil plane to the conventional image plane, and the amplitude of the field propagated is given by $|U_B(\mathbf{x}_P)|$. The propagation from the pupil to the conventional image plane can be accomplished computationally using Fourier transform techniques [21, 24].

The weights obtained from the optimization process are used in Eq. (24) to form the deformable mirror figure associated with the nonlinear optimization algorithm denoted by $\phi_{\text{NL}}^{DM}(i,j)$ In the next section we describe a simulation for propagating a point source beacon field through a turbulent region to a receiving aperture, applying the desired correction to the outgoing beam, and propagating the fields resulting from the three phase correction paradigms used here from the aperture back through the turbulence and on to the beacon plane, where turbulence compensation results can be compared.

3 Simulation description

The algorithm developed here is not linear, and further, we wish to evaluate its performance for saturated scintillation situations. Hence, a simulation was used to evaluate the performance of the new algorithm. The simulation follows the basic conceptual form shown in Fig. 3. The field due to a point source beacon was calculated in the plane of the first phase screen a distance 10 km away from the beacon [24]. The beacon field was propagated through the phase screen using Eq. (15). At each step the field which was passed through the phase screen was propagated 10 km to the next phase screen using an angular spectrum propagator

[21, 24, 7], and the process was repeated until the final screen was encountered in the aperture of the system. A total of 10 random phase screens were used to simulate the 100 km optical path. All of the phase screens and propagations were conducted in 256 × 256 arrays with 1 cm sample spacing. As discussed in Ref. [7], the relationship between the number of points along one edge the fast Fourier transform (FFT) array N, the sample spacing Δx, the wavelength λ, and the propagation distance z is

$$N \geq \frac{2\lambda z}{(\Delta x)^2}.$$ (37)

For the case used here with $\lambda = 987$ nm, $z = 10$ km, and $\Delta x = 1$ cm, using Eq. (37) yields $N \geq 197.4$, so that working with $N = 256$ - sized arrays is satisfactory.

Because a point source beacon emanates waves in all directions it is necessary in a simulation to strongly attenuate rays which are well outside the solid angle subtended from the aperture to the beacon [19]. Attenuating these rays prevents "wrap-around error" which would arise in an FFT-based propagation simulation if these rays were allowed to propagate unattenuated. Our strategy for attenuating these rays is derived from Ref. [19]. Over a region which is 1.5 times the diameter of the circles described by the intersection of the solid angle subtended from the aperture to the beacon and the planes containing the phase screens the beam is allowed to propagate unattenuated. Outside this region a Gaussian rolloff is used to attenuate the field with e^{-1} width of 25 samples. For the propagation from the aperture to the beacon plane the field is converging, and as a result it is not necessary to attenuate the field in this manner.

The phase screens were generated using a white noise filtering approach [19, 20, 30, 31]. Phase screens possessing the von Karman spectrum with outer scale $L_0 = 100$ m were simulated using this method so that ensemble of phase screens has the power spectrum

$$\Phi_\psi(f) = \frac{0.00969k^2 z_l C_n^2}{(f^2 + [1/L_0]^2)^{11/6}},$$ (38)

where f is a spatial frequency with units of inverse meters, and $z_l = 10$ km is the layer thickness. The

26

strength of each screen is controlled by adjusting C_n^2. The phase screens were created in $2N \times 2N$ arrays, and the center $N \times N$ section was extracted to avoid problems arising from the fact that autocorrelation of the phase is an even function [31]. While this approach to phase screen generation has been widely used [19, 20, 30, 31, 32], this approach is known to produce phase screens which are affected by truncation of the power spectrum at both high spatial frequencies, due to finite sample spacing Δx, and at low spatial frequencies, due to finite array size N. We adopt this phase screen generation technique here because of its speed of operation, and because of reasonable agreement between theory and simulation [19].

The beacon field intercepted by the aperture was passed through a simulated lens with complex transmittance given by Eq. (16). The intensity of the beacon field $I_B(\mathbf{x}_P)$ is noted, and used to compute the amplitude of the beacon field $|U_B(\mathbf{x}_P)|$, which is used as the field amplitude in computed propagations to the Hartmann sensor and conventional image planes conducted in the nonlinear optimization-based algorithm. A conventional image $I_C(\mathbf{x}_C)$ and a Hartmann sensor image $I_W(\mathbf{x}_W)$ are computed for each beacon field, and this information is also provided to the nonlinear optimization-based algorithm to compute $\phi_{\mathrm{NL}}^{DM}(i,j)$. A conventional Hartmann sensor centroid-based least squares wave front reconstructor [3] was implemented on the wave front sensor image to obtain $\phi_{\mathrm{LSH}}(i,j)$, and a simulated outgoing laser beam initially carrying the resulting phase was propagated to the beacon plane and evaluated to provide one comparative performance measure for the new algorithm. Point-wise principal value phase differences were also computed for the beacon field using Eqs. (17) and (18), which are input to the branch point phase reconstructor to obtain $\phi_{\mathrm{BP}}(i,j)$ and the ideal least squares reconstructor to obtain $\phi_{\mathrm{LMSE}}(i,j)$. A deformable mirror was fit to $\phi_{\mathrm{BP}}(i,j)$ and $\phi_{\mathrm{LMSE}}(i,j)$ to obtain $\phi_{\mathrm{BP}}^{DM}(i,j)$ and $\phi_{\mathrm{LMSE}}^{DM}(i,j)$, and these phases were applied to the outgoing beam to obtain the branch point and ideal least squares reconstruction results. It should be noted that these pointwise phase differences are an idealization of a real wave front sensor, and would not be available in practice. Hence, these results represent an upper bound on performance that could not be obtained. We provide these results to obtain another comparative measure of performance for the new algorithm.

The outcomes of the four phase correction schemes were associated with an initially planar wave in the aperture to create an outgoing field which was propagated to the beacon plane and evaluated for comparison

27

to the performance of the new algorithm. The outgoing fields were propagated back through the simulated lens and the phase screens, in reverse order, to the beacon plane. In the beacon plane statistical quantities which are used to compute the mean intensities for all of the correction approaches studied. In the absence of turbulence, the intensity pattern in the beacon plane would be an Airy disk [24], but with turbulence and the various correction schemes the actual beacon plane patterns are suboptimal. Statistical quantities required to compute the average far field intensity and the average Strehl ratio were accumulated, where the appropriate definition of Strehl ratio SR for this case is

$$SR = \frac{\text{Actual on-axis intensity}}{\text{On-axis intensity with no atmosphere}}. \tag{39}$$

We also computed the radial average of the intensity patterns in the beacon plane. We now detail the physical parameters used in the simulation.

A 0.5 m diameter receive/transmit aperture was modeled, and the wavelength of operation was set at 987 nm. Deformable mirror actuators were placed on a Cartesian grid with spacing of 8 cm in the plane of the receive/transmit aperture, providing for a total of 37 actuators. Deformable mirror influence functions were implemented as described in Eq. (20). When equal weights are applied to all actuators in this configuration a planar deformable mirror figure results. The wave front sensor had 8 subapertures across its diameter for a total of 35 fully illuminated subapertures within the pupil. This arrangement of actuators and subapertures provides a stable solution to Eq. (30). When projected into the pupil plane the subapertures had side length equal to 6 cm, though they were actually modeled as having physical side length of 90 μm and focal length of 3 mm. The sample spacing in the wave front sensor lenslet and detector planes was 15 μm, satisfying the sampling criterion for the wave front sensor lenslet array [21]

$$\Delta x_W \leq \frac{2\lambda f_l}{3d}, \tag{40}$$

where Δx_W is the sample spacing in the wave front sensor plane since $\Delta x_W = 15\mu$m $\leq 21.9\mu$m. The image

plane for each subaperture occupied a 7 × 7 sample region behind each lenslet. A Monte Carlo simulation approach was used, with 50 statistically independent propagations used to obtain the results presented.

The simulation can be evaluated by comparing the theoretical Rytov variance $\sigma^2_{\chi,R}$ calculated using Eq. (13) to the variance of the log amplitude fluctuations σ^2_{χ} at the aperture calculated from a set of 100 simulated propagations through the turbulent volume. This plot is shown in Fig. 6, where the $\sigma^2_{\chi,R}$ and the simulated σ^2_{χ} are plotted as a function of C^2_n for the path. Inspection of Fig. 6 shows that the simulation consistently provides slightly stronger values of σ^2_{χ} than are be predicted by Eq. (13) when $\sigma^2_{\chi,R} \leq 0.3$, and the σ^2_{χ} provided in the simulation saturates, as expected [17, 19], at $\sigma^2_{\chi} \approx 0.35$. The fact that simulated σ^2_{χ} is larger than $\sigma^2_{\chi,R}$ for low values of $\sigma^2_{\chi,R}$ most likely arises from the attenuation of the rays implemented to avoid wrap-around error discussed above, and the limitations of the phase screen generator, also discussed above.

4   Theoretical and simulation results.

Results of this study are presented in Figs. 7 and 8. Figure 7 shows radial averages of the far field intensity patterns for the $C^2_n = 3 \times 10^{-17}$ case, where the peak intensity has been normalized to the intensity obtained by the branch point reconstruction technique. In this case the Rytov variance is 0.47, and saturated log amplitude fluctuations were obtained in the simulation. Inspection of Fig. 7 shows that the branch point reconstructor performed significantly better than the least squares reconstructor, a consistent result for all cases where saturated log amplitude fluctuations arose.

Figure 8 shows SR vs. C^2_n and SR vs. the Rytov variance for all of the simulation runs conducted. Inspection of Fig. 8 shows that for low values of Rytov variance, or equivalently, low values of C^2_n, the branch point and least squares recontructors perform comparably. However, in the region where the log amplitude fluctuations are saturated, $\sigma^2_{\chi} > 0.35$, branch point reconstruction has a significant advantage in Strehl ratio over least squares reconstruction. These results demonstrate the importance of branch point reconstruction for adaptive optical laser beam propagation through the atmosphere for optical paths that cause saturated
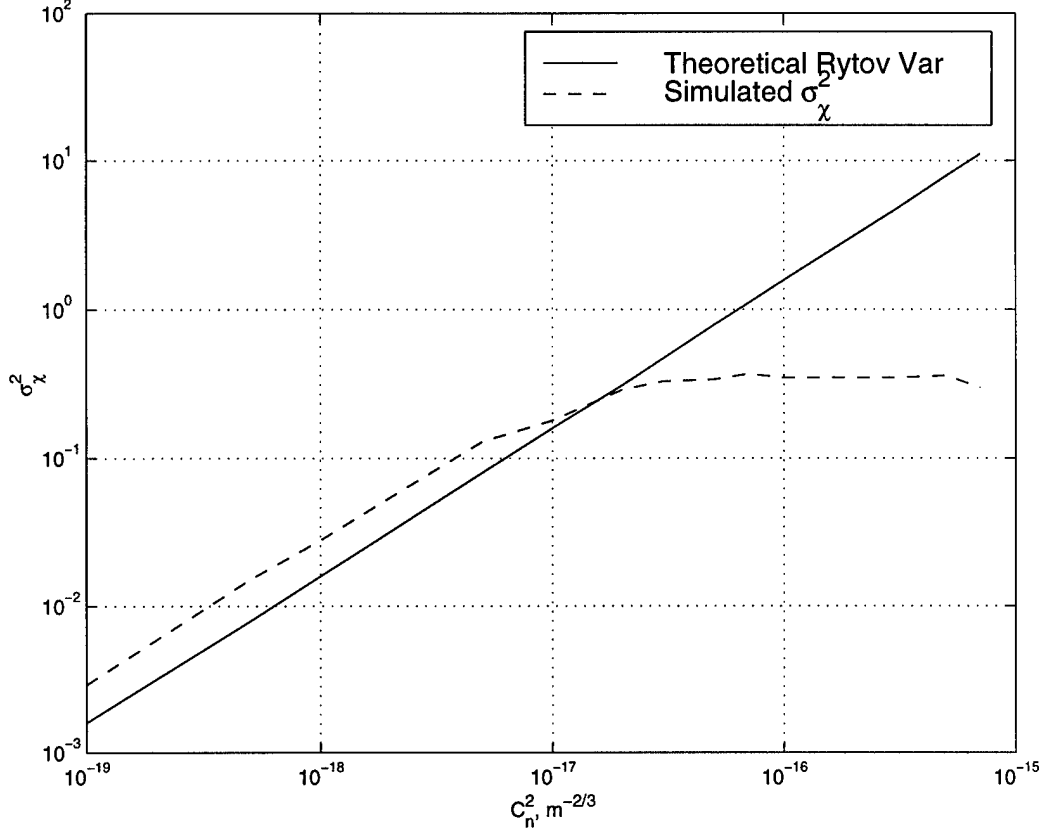
Figure 6: Theoretical Rytov variance, and simulated σ_χ^2 as a function of C_n^2.

log amplitude fluctuations. Further, these results show that fitting errors between the deformable mirror and the discontinuous branch point reconstructed phase do not dominate the errors in the outgoing beam.

The main results of this paper are presented in Figs. 9 and 10. The input C_n^2 values, the associated Rytov variances $\sigma_{\chi,R}^2$, and the average number of objective function evaluations required convergence N_I are listed in Table 1. In the legends of both these figures "BP" refers results obtained for $\phi_{BP}^{DM}(i,j)$, "LS" refers to results obtained for $\phi_{LS}^{DM}(i,j)$, "WFS" refers to results obtained with $\phi_{LSH}^{DM}(i,j)$, and "NL OPT" refers to results obtained with $\phi_{NL}^{DM}(i,j)$. Results for the curves labeled BP and LS are unobtainable in practice because they require that pointwise phase differences be available, and these curves are provided for purposes of comparison. The curves labeled WFS and NL OPT are, in principle, obtainable in practice since they can be computed from intensity information available in an adaptive optical system. The branch point
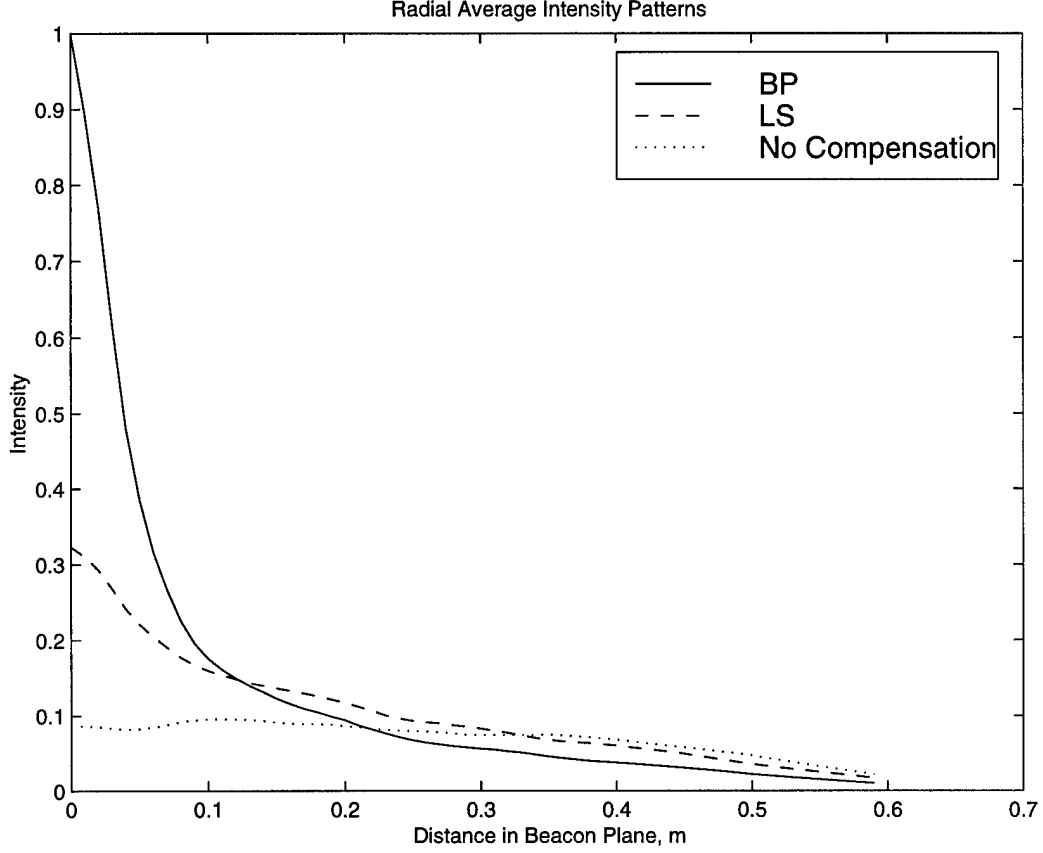
Figure 7: Radial averaged far field intensity patterns for the case $C_n^2 = 3 \times 10^{-17}$.

reconstruction results represent the upper bound on performance for the nonlinear optimization technique, and the idealized least squares curves represent an upper bound on the performance of the Hartmann sensor-based least squares reconstruction technique.

Figure 9 shows the average Strehl ratio results for the four correction techniques investigated. For $7 \times 10^{-18} \leq C_n^2 < 1 \times 10^{-17}$ scintillation is weak, and using conventional Hartmann sensor processing provides better Strehl ratio performance than the nonlinear optimization technique. However, as $\sigma_{\chi,R}^2$ increases, the nonlinear optimization technique begins to outperform the conventional Hartmann sensor processing approach. The onset of saturated scintillation occurs in the vicinity of $C_n^2 = 2 \times 10^{-17}$ for the geometry studied here. In the regime $C_n^2 > 2 \times 10^{-17}$ the nonlinear optimization technique provides Strehl
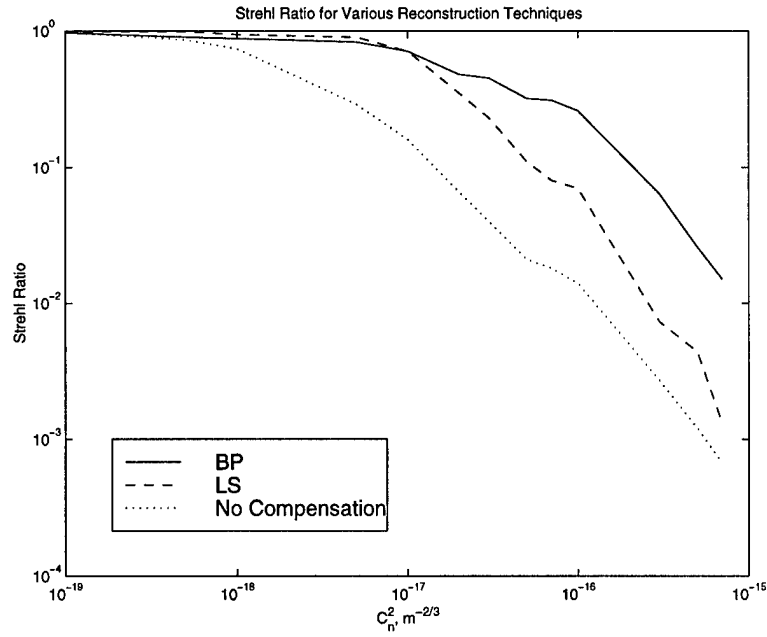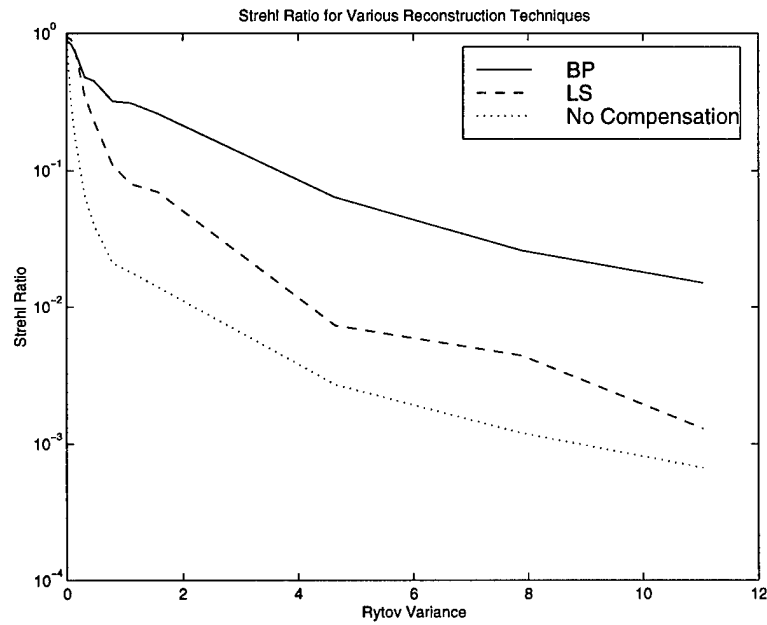
Figure 8: Strehl ratio results for branch point and least squares reconstruction, and for no compensation: (a) Strehl ratio vs. C_n^2; and (b) Strehl ratio vs. Rytov variance $\sigma_{\chi,R}^2$.

Table 1: Listing of C_n^2, $\sigma_{\chi,R}^2$, and N_I for the plots shown in Figs. 9 and 10.

C_n^2	$\sigma_{\chi,R}^2$	N_I
7×10^{-18}	0.11	44.5
1×10^{-17}	0.16	49.9
2×10^{-17}	0.32	53.6
3×10^{-17}	0.47	57.5
4×10^{-17}	0.63	56.8
5×10^{-17}	0.79	58.5
6×10^{-17}	0.95	53.6
7×10^{-17}	1.10	57.0
8×10^{-17}	1.26	53.1
9×10^{-17}	1.42	51.5
1×10^{-16}	1.58	50.1

ratios which are a factor of 1.5 to 4 larger than those provided by conventional Hartmann sensor processing.

The radially averaged intensity patterns shown in Fig. 10 were computed by averaging the beacon plane intensity for the projected beam, and then averaging this result over circles of constant radius. These plots indicate that the nonlinear optimization approach provided results superior to the conventional Hartmann sensor-based approach for all cases of saturated scintillation in both on-axis intensity, and by providing narrower beam width. In fact, the nonlinear optimization technique for wave front control yields results which approach those provided by the idealized branch point reconstruction technique.
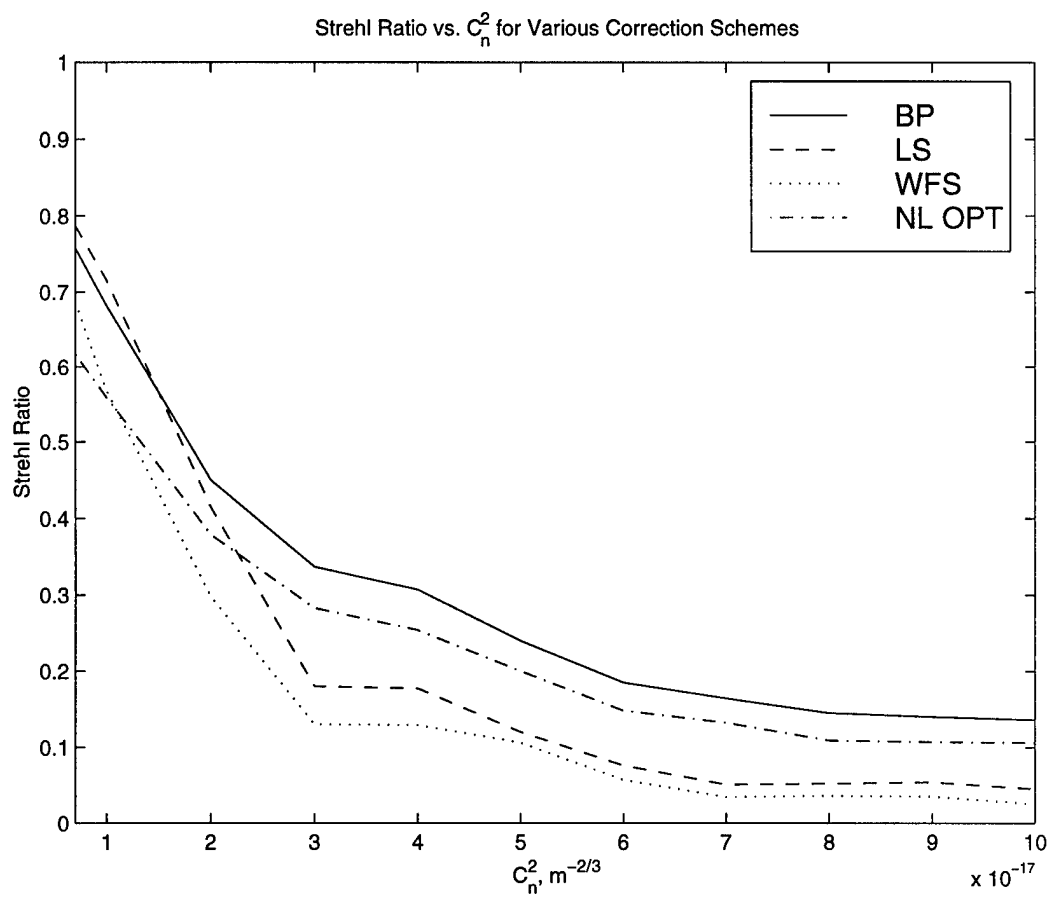
Figure 9: Strehl ratio results for the various correction schemes. In the legend "BP" refers results obtained for $\phi_{BP}^{DM}(i,j)$, "LS" refers to results obtained for $\phi_{LS}^{DM}(i,j)$, "WFS" refers to results obtained with $\phi_{LSH}^{DM}(i,j)$, and "NL OPT" refers to results obtained with $\phi_{NL}^{DM}(i,j)$.

34
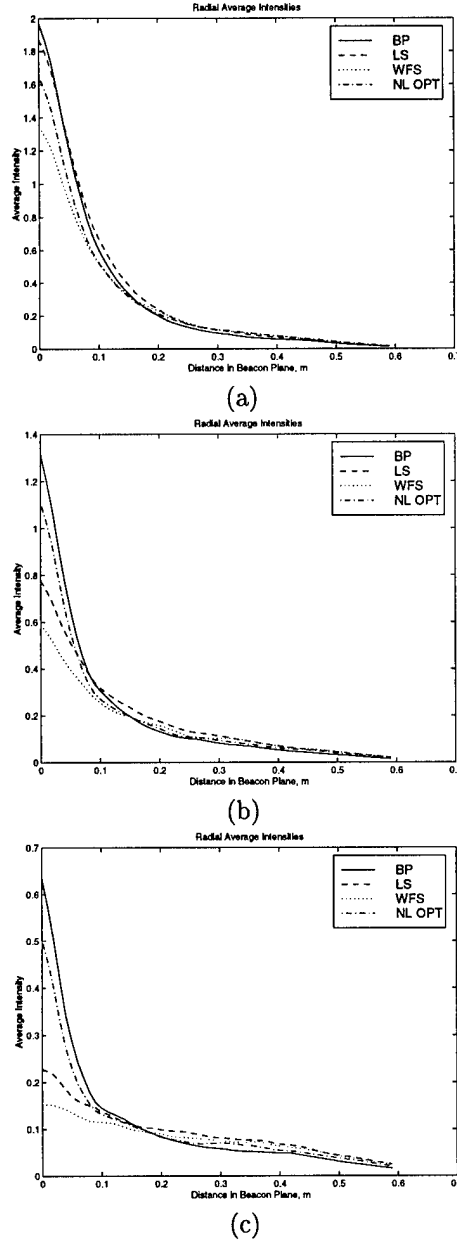
Figure 10: Example radially averaged beacon plane intensities for the projected beam: (a) $C_n^2 = 2 \times 10^{-17}$, $\sigma_\chi^2 = 0.316$; (b) $C_n^2 = 4 \times 10^{-17}$, $\sigma_\chi^2 = 0.631$; and (c) $C_n^2 = 7 \times 10^{-17}$, $\sigma_\chi^2 = 1.104$. In the legend "BP" refers results obtained for $\phi_{BP}^{DM}(i,j)$, "LS" refers to results obtained for $\phi_{LS}^{DM}(i,j)$, "WFS" refers to results obtained with $\phi_{LSH}^{DM}(i,j)$, and "NL OPT" refers to results obtained with $\phi_{NL}^{DM}(i,j)$.

5   Experiment and experimental results.

An experiment has been set up and designed to verify the ability to control the amplitude of the transmitted wave front field falling on the DM_2 in the two-deformable-mirror concept. In the experiment, a collimated laser beam illuminates a deformable mirror which was controlled electronically. A wave front sensor (WFS) measurement of the wave front field reflected from the deformable mirror is taken by a digital camera. The WFS measurement is used to obtain the phase of the reflected wave front field. A Fourier-transforming lens is used to obtain the Fraunhofer diffraction or far field intensity of the reflected wave front field. The Fraunhofer diffraction pattern of the reflected wave front field is the amplitude of the transmitted wave front field falling on DM_2 in the two-deformable-mirror concept. The far field intensity of the reflected wave front field is measured by a digital camera. The far field intensity pattern is compared with the theoretical far field pattern. The theoretical far field intensity pattern is obtained by taking the Fourier transform of $\exp\{j\psi_1(\vec{x})\}$, where $\psi_1(\vec{x})$ represents the reconstructed phase from the WFS measurement. In the experiment, a good match was obtained between the measured intensity pattern and the intensity pattern predicted from the Hartmann sensor measurement.

The nonlinear response and strong coupling of control channels in the deformable mirror make the deformable mirror used here difficult to drive to a desired surface shape [33, 34]. Each actuator produces an electrostatic force to push or pull the mirror surface to form a particular mirror surface shape, and each actuator modulates the whole surface of the mirror. Therefore, no linear relationship between the control signals and the exact deformation of the mirror exists.

The deformable mirror used in the experiment is the micromachined membrane deformable mirror (MMDM) from OKO technologies [34, 35]. MMDM consists of silicon chip mounted over a PCB holder. The chip contains silicon nitride membrane, which is coated with aluminum to form the mirror. The PCB contains the control electrode structure, spacer, and connector. The design of the assembled mirror is shown in Fig 11. The MMDM consists of 37 actuators which drive the deformable mirror surface. A layout of the MMDM actuators is shown in Fig. 12. The shape of the reflective membrane is controlled by applying volt-

ages between the membrane and the control electrodes. These control voltages are supplied by 8 bit digital boards installed in a computer and two identical high-voltage DC amplifier boards. The output voltages of the digital board are in the range from 1 to 3.65 V. The range of the output voltage has been digitized between 0 and 255. Then, the output voltages are sent to two identical high-voltage amplifier boards. Each board contains 20 non-inverting DC amplifiers. Each amplifier has a gain 59, providing the output voltage swing of 1 to 213 V. The amplified output voltages are sent to MMDM and drive the deformable mirror surface.

The nonlinear response and strong coupling of control channels in the deformable mirror make this deformable mirror difficult to drive to a desired surface shape [33, 34]. Each actuator will produce an electrostatic force to push or pull the mirror surface. The force produce by each actuator is defined as:

$$F = \frac{\epsilon \epsilon_o (V_b + V_c)^2 S}{d^2},$$ (41)

where $\epsilon \epsilon_o$ is the dielectric constant of the material between the electrodes (air), S is the area of the electrode, d is the distance between the electrodes, V_b is the bias voltage and V_c is the control voltage. Each actuator modulates the whole surface of the mirror. The overall mirror surface deformation has a nonlinear response. The strong coupling of control channel is presented because the actuators are close to each other, and due to the mechanical properties of the surface material. Therefore, we were unable to estimate the relationship between the control signals and the exact deformation of the mirror. The control signals can be found from the wave front phase by the least squares phase reconstruction technique [3].

An influence function and the corresponding WFS image are shown in Fig. 13. The influence function is obtained by applying voltage level 255 to actuator 2 and 64 to other actuators. During the phase reconstruction, only center 980×980 pixels are used from the WFS image. Also, the influence function 1, 19 and 37 are shown in Fig. 14. A calibration phase is obtained by replacing the deformable mirror with the flat mirror. This calibration phase is the deterministic phase error caused by the deterministic tilt in the wave front field, and is subtracted from each reconstructed phase. The calibration phase and the corresponding

Table 2: Focal lengths of lenses used in the experiment setup.

Lens label	Focal length (mm)
L_o	400
L_i	175
L_{FT}	500
L_{TL}	75.6

Table 3: Nominal distances used in the experiment setup.

Element Separation	Distance (mm)
Iris to Center of Beam Splitter I	145
Center of Beam Splitter I to Center of Beam Splitter II	207
Center of Beam Splitter II to Deformable Mirror	220
Center of Beam Splitter II to L_o	173
L_o to L_i	608
L_i to Hartmann Lenslet Array	193
Hartmann Lenslet Array to Hamamatsu Digital Camera	26
Center of Beam Splitter I to L_{FT}	97
L_{FT} to Turning Mirror	330
Turning Mirror to L_{TL}	320
L_{TL} to Cohu Digital Camera	310

WFS image are shown in Fig. 15.

In order to apply the phase deformation to DM_1 and DM_2, a set of actuator commands are sent to the DM_1 and DM_2. The actuator commands can be obtained by using the least squares phase reconstruction technique [3, pages 177–197]. The ith influence function is obtained by applying the voltage level 255 to the ith actuator and 64 to other actuators.

An experiment was designed to verify the ability to control the amplitude of the wave front field falling on the DM_2 in the two-deformable-mirror concept. The block diagram of the experimental setup for controlling the amplitude falling on the DM_2 is shown in Fig. 16. Lens focal lengths and nominal positioning dimensions in the experiment setup are summarized in Table 2 and 3.

A 17 mW He-Ne laser beam with λ=632.8 nm was used as a light source. The laser beam passed through the neutral-density filter. The neutral-density filter is used to reduce the intensity of the laser beam. The laser beam after the neutral-density filter passed through a beam expander. The purpose of the beam

expander is to generate an expanded and collimated laser beam. Then, the expanded and collimated laser beam passed through an iris to reduce the diameter of the laser beam to 15 mm. The laser beam after the iris illuminated on the Beam Splitter I. The Beam Splitter I directed the laser beam to Beam Splitter II. The Beam Splitter II directed the laser beam to the deformable mirror. A wave front field is reflected from the deformable mirror. The deformable mirror is the micromachined membrane deformable mirror (MMDM) from OKO Technologies [35]. The reflected wave front field is reflected back to Beam Splitter II. Beam Splitter II sends half of the wave front toward the afocal telescope and half of the wave front to Beam Splitter I. The afocal telescope is formed by two convex lens. The purpose of the afocal telescope is to reduce the diameter of the beam from 15mm to 6.56mm. The mathematical expression for the beam diameter reduction caused by an afocal telescope is represented as follow:

$$d_2 = \left(\frac{f_2}{f_1}\right) d_1, \tag{42}$$

where d_2 is the diameter of the wave front field after the afocal telescope, d_1 is the diameter of the wave front field before the afocal telescope, f_1 is the focal length of the lens L_o and f_2 is the focal length of the lens L_i. In the experiment, d_2 is 6.56 mm, d_1 is 15 mm, f_1 is 400 mm and f_2 is 175 mm. The compacted wave front field is passed to the lenslet array. The lenslet array segments the wave front field and focusses the light on the detector plane of the Hamamatsu digital camera. Each lenslet of the lenslet array has focal length = 24 mm and side length = 328 μm. Hence, there were 20 subapertures across the beam diameter. The model number of the Hamamatsu digital camera is C4742-95. The detector plane of the Hamamatsu digital camera consists of a 1024×1024 pixel array, and the rectangular pixels have dimensions of 6.7 μm×6.7 μm. A WFS image is taken by the Hamamatsu digital camera. The WFS image is processed by the phase reconstruction software to reconstruct the wave front phase. The theoretical far field intensity can be computed by the following expression

$$I_{th} = |FT[\exp\{j\psi_1(\vec{x})\}]|^2 \tag{43}$$

where $FT[\cdot]$ is the Fourier transform operator and $\psi_1(\vec{x})$ is the reconstructed phase.

The dynamic range of Fourier spectrum predicted by Eq. (43) is higher than the dynamic range of the detector in the Cohu digital camera [36, pages 92–93]. Hence, only the brightest part of the far field intensity which computed from Eq. (43) is visible. In order to see the far field intensity in detail, the theoretical far field intensity can be computed by the mathematical function [36],

$$I_{ex} = \log(I_{th} + 10000) \tag{44}$$

The logarithm function is used to reduce the dynamic range of the far field intensity.

The other half of the wave front field from Beam Splitter II passed through Beam Splitter I and fell on the lens L_{FT} with f=500 mm. This lens is the Fourier-transforming lens in the two-deformable-mirror concept. The wave front field after the lens was passed toward the turning mirror. The reason for using the turning mirror is to create more space on the optical bench. The wave front field reflected from the turning mirror is propagated through two neutral-density filters to avoid saturation the detector. A positive lens L_{TL} with f=75.6 mm is used to magnify the far field image. The ratio of the magnification is 3:1. The thin lens law is used to achieve the magnification. From the thin lens law,

$$M = -\frac{s_i}{s_o}, \tag{45}$$

and

$$\frac{1}{s_i} + \frac{1}{s_o} = \frac{1}{f}, \tag{46}$$

where "−" sign indicate the image is inverted, M is the magnification, s_i is the image distance, s_o is the object distance and f is the focal length of the lens which used in the magnification system. In the experiment, f is 75.6mm. The s_i and s_o cannot be measured exactly from the experiment because the plane of the lens cannot be located. A variable neutral-density filter wheel is placed in front of the Cohu digital camera to control exposure on the detector plane of the Cohu digital camera, which had a fixed integration time of 33 ms. The model number of the Cohu digital camera is 4110. The image plane has 480×752 pixels, and the

rectangular pixels have dimensions of 8.66 μm$\times$9.92 μm.

The location of focus of both digital cameras can be found by counting the number of pixels between the first zeros of the point spread functions with the deformable mirror replaced by a flat mirror. The deformable mirror is not used for alignment because deformable mirror surface is not flat. The deformable mirror has initial deviation from plane of less than 0.6 μm [35]. In the case of finding the location of focus of Cohu digital camera, the diameter of the laser beam was reduced to 8mm from 15 mm to broaden the Airy disk, making it easier to find focus. The width between the first zeros of the point-spread functions on the Cohu digital camera can be calculated by the following expression:

$$\text{width} = \frac{2.44 M f \lambda}{D} \qquad (47)$$

where M is the magnification of the image, f is the focal length of the Fourier-transforming mirror, λ is the wavelength of the laser beam and D is the diameter of the laser beam. In the experiment, M=3, f=500 mm, λ=632.8 nm and D=8 mm. Therefore, the width between the first zeros of the point-spread functions on the Cohu digital camera is 289.51 μm. The number of pixels which span the x-axis slice of the point spread function on the detector plane is thus 33 pixels. From the experiment, we found that the number of pixels in the x-axis slice of the point spread function is 34 pixels. The picture and the x-axis slice of the point spread function are shown in Fig. 17 and Fig. 18. Finally, the far field intensity is measured and displayed on the Cohu digital camera.

In order to test the performance of the experiment, different sets of micromachined membrane deformable mirror actuator voltage signals are applied to drive the mirror to different surface shapes. In a particular set of mirror actuator voltage signals, a WFS image on the Hamamatsu digital camera and a far field intensity on the Cohu digital camera are measured. The phase of the wave front field reflected from the deformable mirror is reconstructed from the wave front sensor measurement. The measured far field intensity pattern can be compared with the theoretical intensity far field pattern. In order to compare the measured far field intensity pattern and the theoretical far field intensity pattern, same spacing in both image are required.

41

The measured far field intensity pattern has been interpolated by using the bicubic interpolation to have same spacing with the theoretical far field intensity pattern. Both far field intensity patterns have 256×256 pixel array, and the rectangular pixels have dimensions of 48.04 μm×48.04 μm.

The experiment results shown in Fig. 20 are obtained by applying the maximum voltage (in digitized levels) of 255 to actuators one and two, and constant voltage 64 on the other actuators. Figure 20(a) show the reconstructed phase, Fig. 20(b) shows the theoretical far field intensity pattern, and Fig. 20(c) shows the measured far field intensity pattern on the Cohu digital camera.

The experiment results that shown in Fig. 21 is obtained by applying the maximum voltage of 255 (in digitized levels) to actuator 1, 19 and 37, and the constant voltage 64 to the other actuators. Fig. 21(a) shows the reconstructed phase, Fig. 21(b) shows the theoretical far field intensity pattern, and Fig. 21(c) shows the measured far field intensity pattern on the Cohu digital camera.

From the experiment results above, the far field intensity pattern is successfully obtained. This far field intensity is the intensity of the transmitted wave front field falling on the DM_2 in the two-deformable-mirror concept. The ringing effect present in all theoretical far field intensity patterns is due to the two-dimensional triangle function which were used as elementary functions in phase reconstruction.

6   Conclusions

In this program the problem of correcting for atmospheric turbulence-induced scintillation errors in laser beam projection and imaging through the atmosphere has been addressed. The approach taken was the implementation and study of a phase and amplitude correction technique which uses two deformable mirrors, and then extend these results to look at a novel algorithm for controlling a single deformable mirror. This work has been successful in that it has been demonstrated that the possibility of compensating for turbulence-induced scintillation exists for both the laser beam projection and imaging applications. Studies of the implications of using real adaptive optical system hardware to implement the two deformable mirror technique have shown the limitations of this approach. However, the results obtained here for the nonlinear

optimization-based approach to controlling a single deformable mirror show a great deal of promise, and will
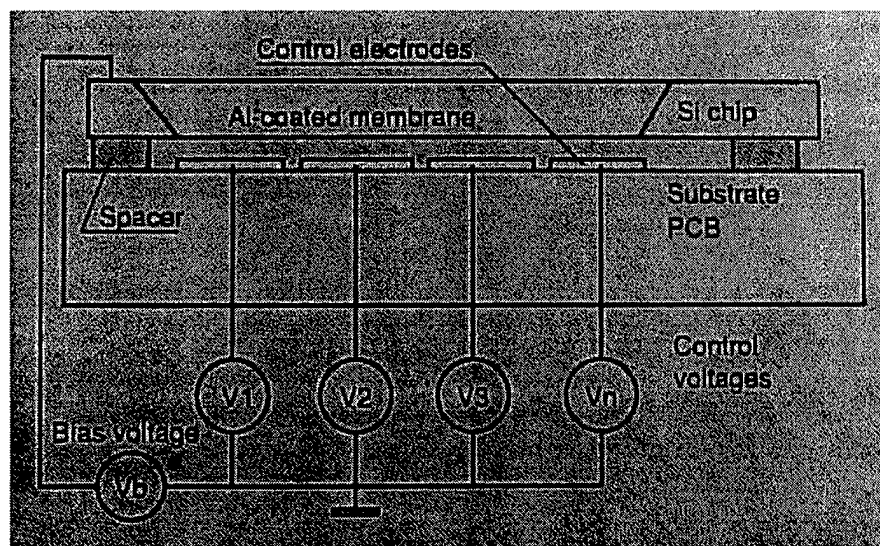
be pursued in the future.

Figure 11: The schematic diagram of the micromachined membrane deformable mirror.
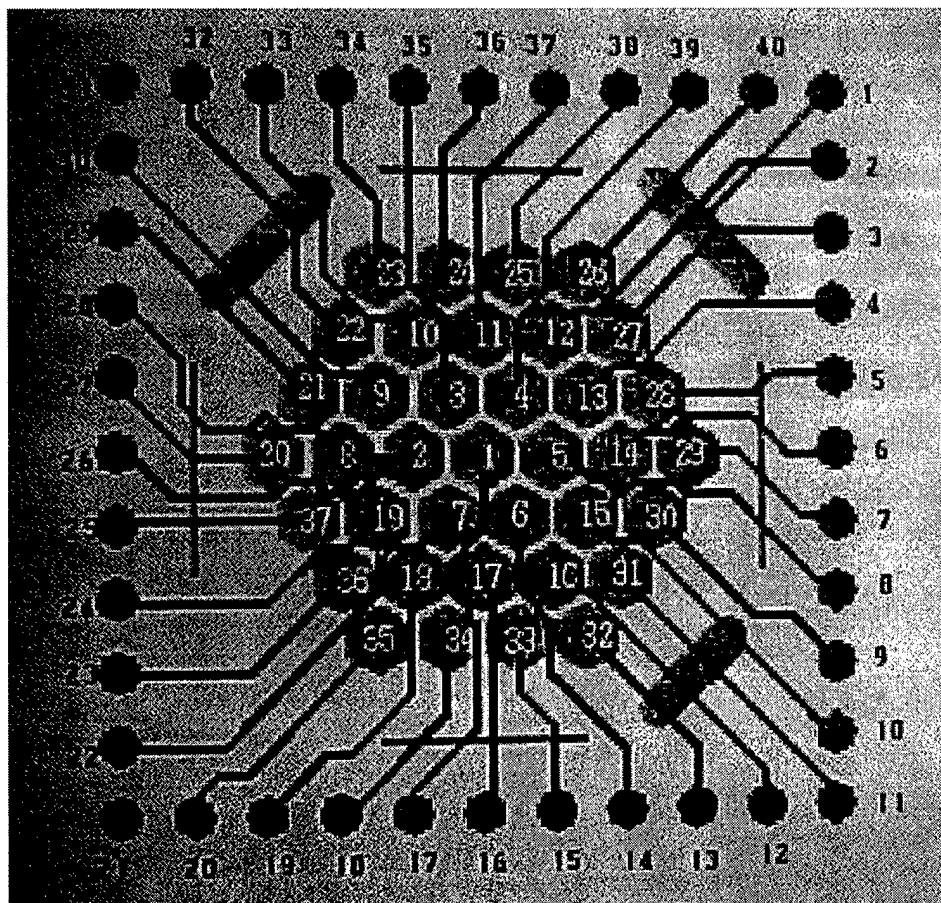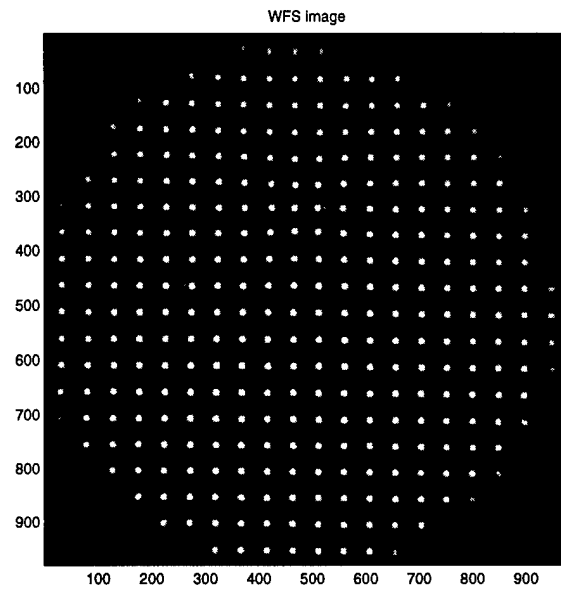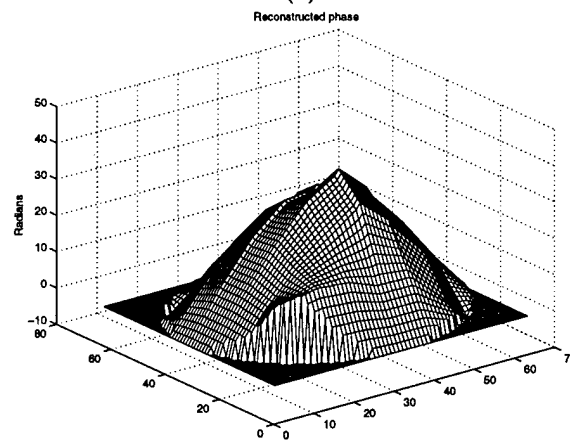
Figure 12: The actuator layout on the micromachined membrane deformable mirror.

WFS image

Reconstructed phase

Figure 13: (a) WFS image (b) The influence function; with applying voltage level 255 to actuator 2 and 64 to other actuators of the deformable mirror.
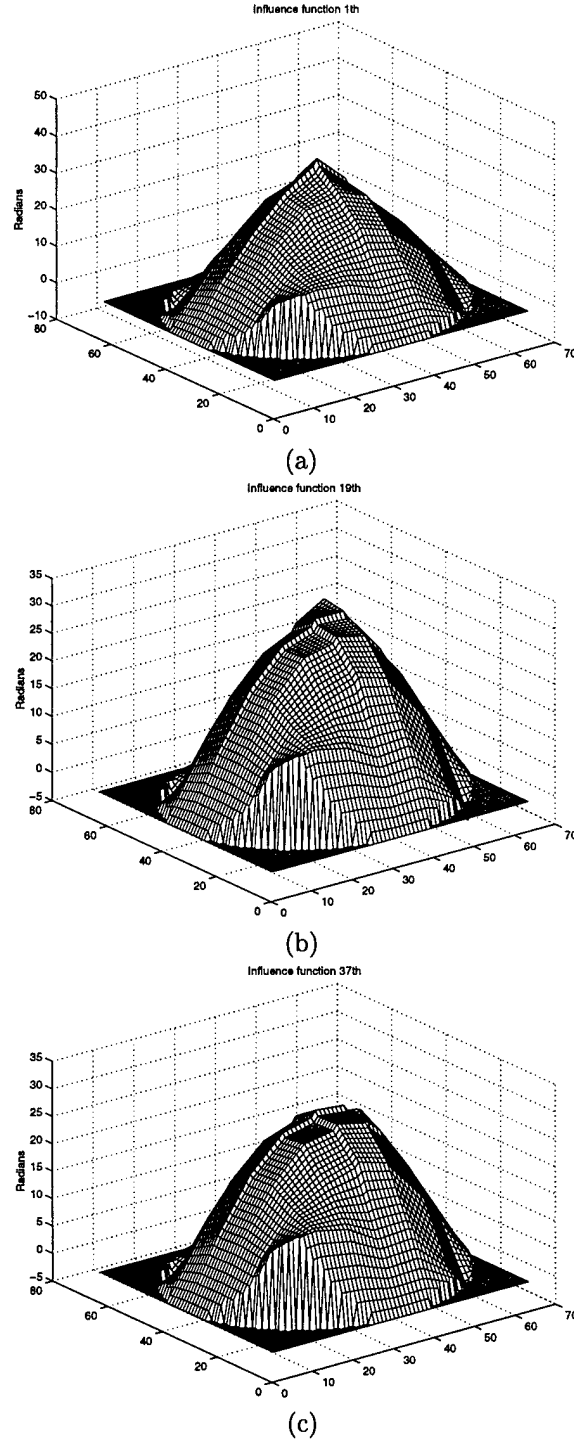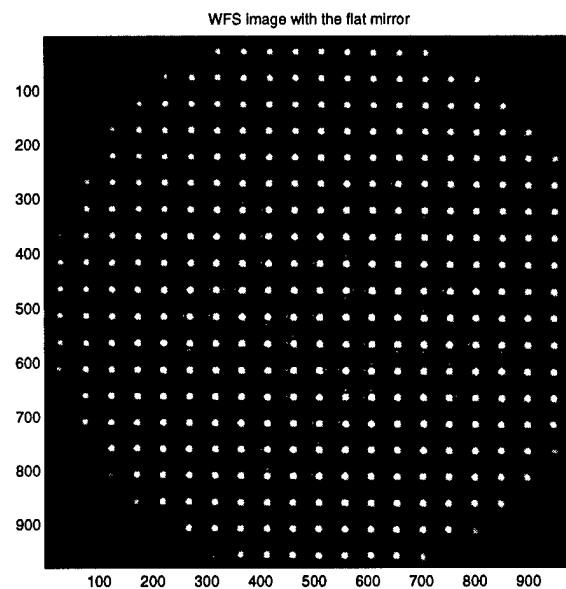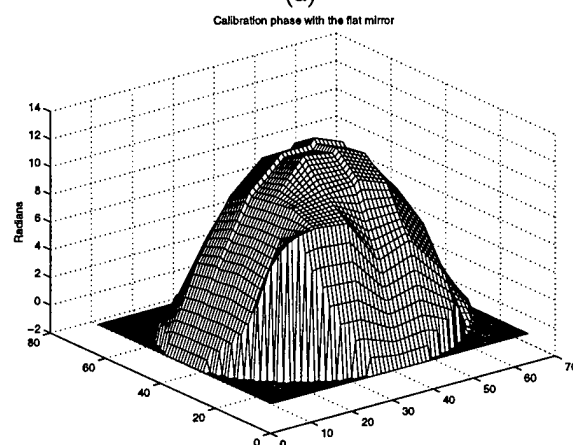
Figure 14: The influence functions are obtained by applying, maximum voltage 255 on actuator l^{th}, and constant voltage 64 on the other actuators: (a) The influence function 1. (b) The influence function 19. (c) The influence function 37.

WFS image with the flat mirror

(a)

Calibration phase with the flat mirror

(b)

Figure 15: (a) WFS image (b) The calibration phase; with the deformable mirror replaced by flat mirror.

48
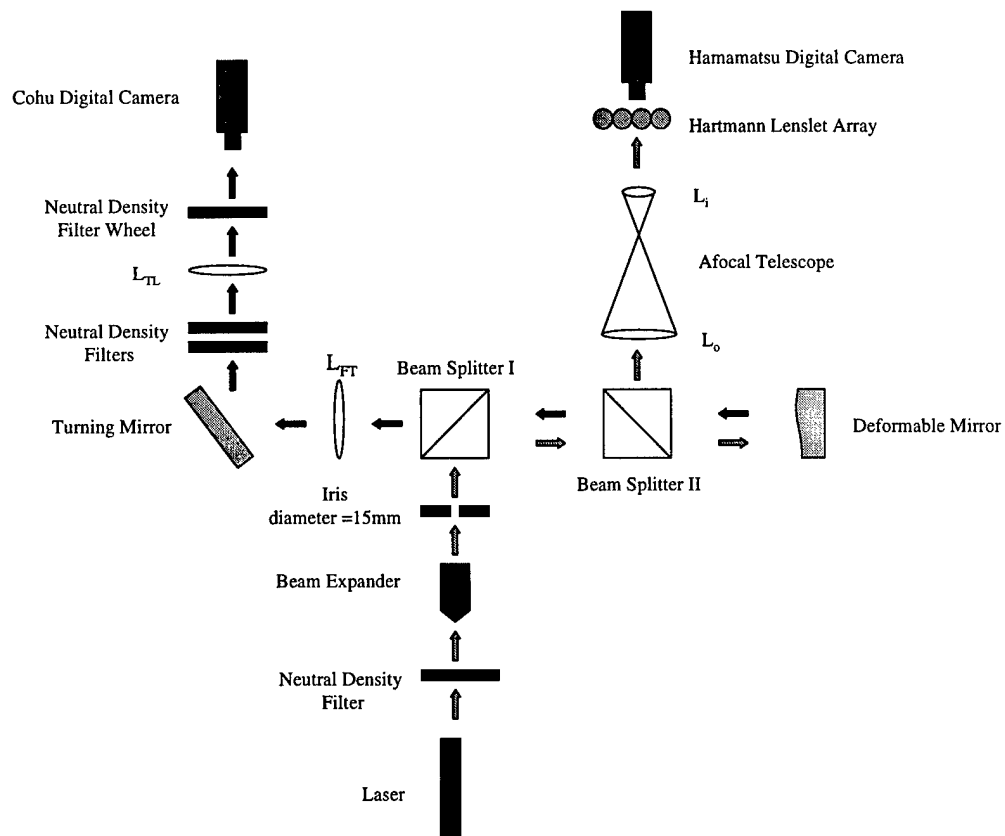
Figure 16: Block diagram of the experimental setup for controlling the amplitude falling on DM_2.
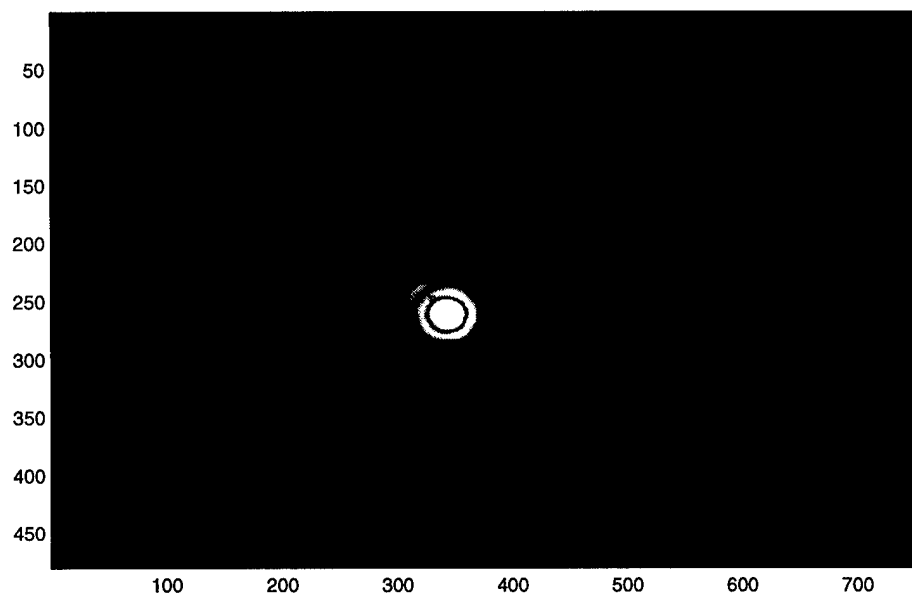
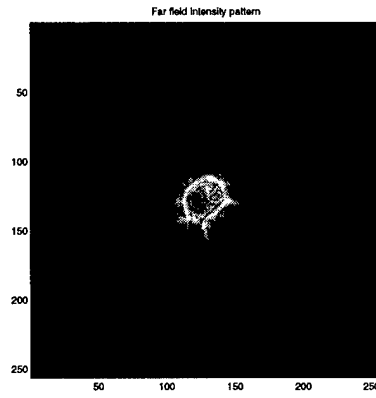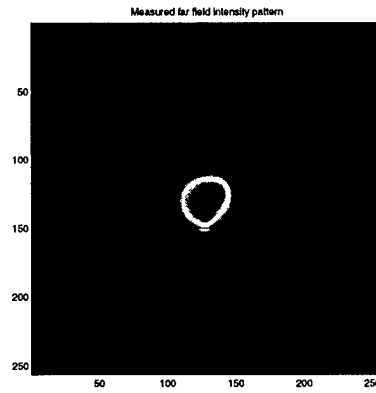Figure 17: The point spread function with the flat mirror falling on the Cohu digital camera.
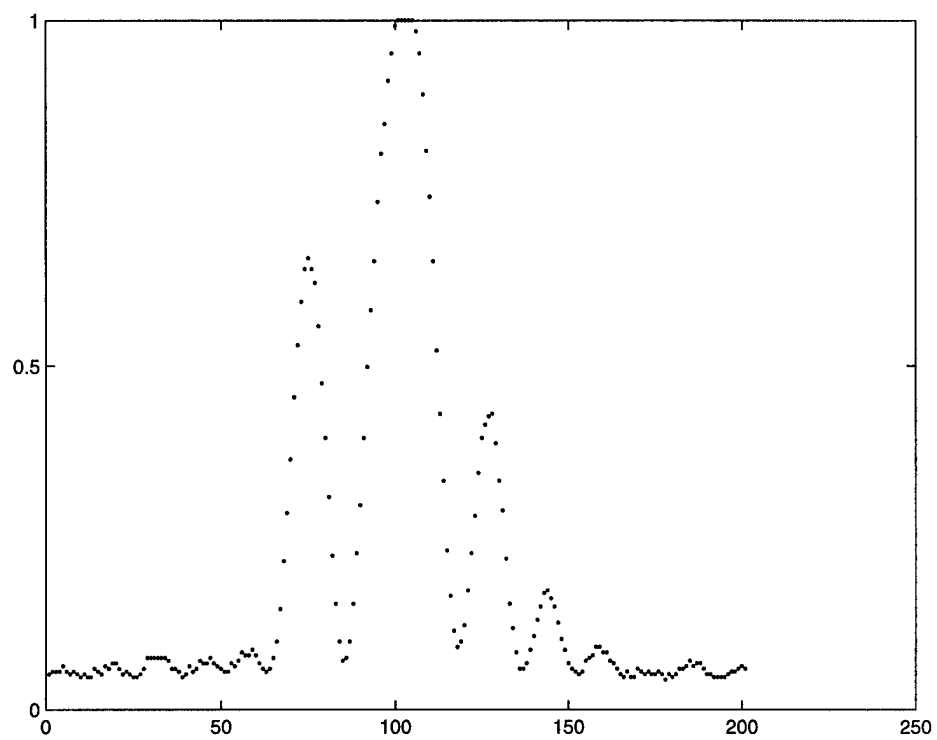
Figure 18: The x-axis slice of point spread function with the flat mirror falling on the Cohu digital camera.
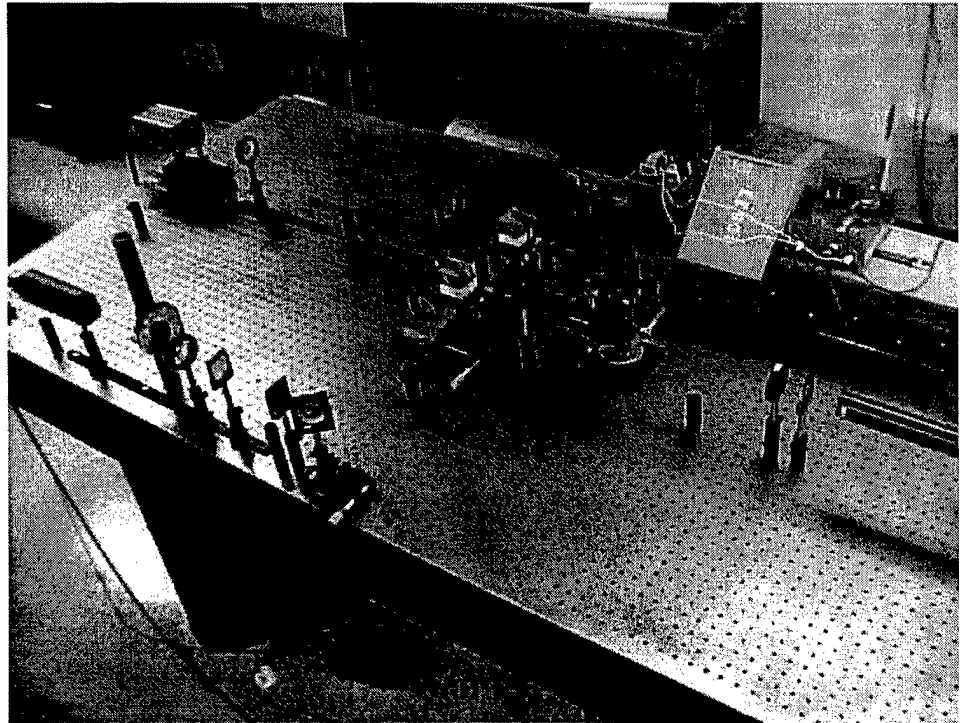
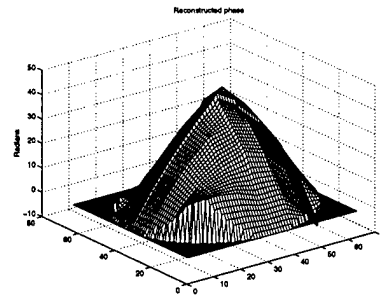Figure 19: Photograph of the experiment setup.
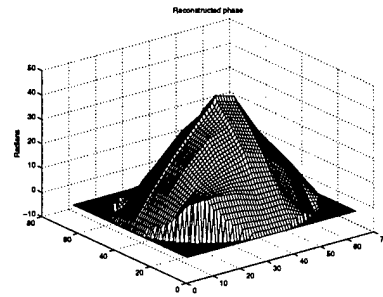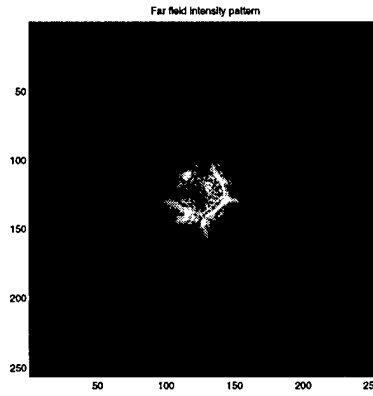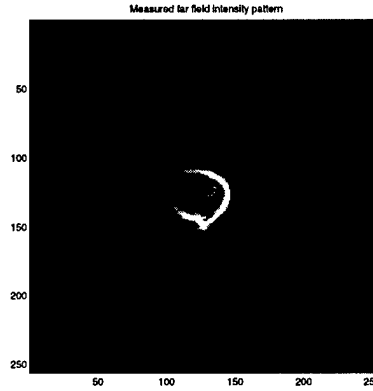
(a)

(b)

(c)

Figure 20: The experiment results is obtained by applying the maximum voltage of 255 (in digitized levels) on actuators one and two, and the constant voltage of 64 on the other actuators: (a) Reconstructed phase; (b) theoretical far field intensity pattern; (c) measured far field intensity pattern

(a)

(b)

(c)

Figure 21: The experimental results obtained by applying, the maximum voltage of 255 (in digitized levels) to actuator 1, 19 and 37, and constant voltage 64 to the other actuators: (a) Reconstructed phase; (b) theoretical far field intensity pattern; (c) measured far field intensity pattern

References

[1] R. W. Lee and J. C. Harp, "Weak scattering in random media, with applications to remote probing," *Proc. IEEE*, vol. 57, pp. 375–406, 1969.

[2] J. W. Goodman, *Statistical Optics*. New York: John Wiley & Sons, 1985.

[3] M. C. Roggemann and B. M. Welsh, *Imaging Through Turbulence*. Boca Raton, FL: CRC Press, 1996.

[4] V. P. Lukin, *Atmospheric Adaptive Optics*. Bellingham, WA: SPIE Press, 1995.

[5] R. Q. Fugate, B. L. Ellerbroek, C. H. Higgins, M. P. Jelonek, W. J. Lange, A. C. Slavin, W. J. Wild, D. M. Winker, J. M. Wynia, J. M. Spinhirne, B. R. Boeke, R. E. Ruane, J. F. Moroney, M. D. Oliker, D. W. Sindle, and R. A. Cleis, "Two generations of laser-guide-star adaptive-optics experiments at the Starfire Optical Range," *J. Opt. Soc. Am. A*, vol. 11, pp. 310–314, 1994.

[6] G. D. Love, J. S. Fender, and S. R. Restaino, "Adaptive wavefront shaping with liquid crystals," *Optics & Photonics News*, vol. 6, pp. 16–21, 1995.

[7] M. C. Roggemann and D. J. Lee, "Two deformable mirror concept for correcting scintillation effects in laser beam projection through the turbulent atmosphere," *Appl. Opt.*, vol. 37, pp. 4577–4585, 1998.

[8] Y. Kanev and V. P. Lukin, "Amplitude phase beam control with the help of a two-mirror adaptive system," *Atm. Opt.*, vol. 4, pp. 878–881, 1991.

[9] F. Y. Kanev and V. P. Lukin, "Algorithms of compensation for thermal blooming," *Atm. Opt.*, vol. 4, pp. 856–863, 1991.

[10] V. P. Lukin, B. V. Fortes, F. Y. Kanev, and P. A. Konyaev, "Potential capabilities of adaptive-optical systems in the atmosphere," *J. Opt. Soc. Am. A*, vol. 11, pp. 903–907, 1994.

[11] N. C. Gallagher and B. Liu, "Method for computing kinoforms that reduces image reconstruction error," *Appl. Opt.*, vol. 12, pp. 2328–2335, 1973.

[12] M. T. Eismann, A. M. Tai, and J. N. Cederquist, "Iterative design of a holographic beamformer," *Appl. Opt.*, vol. 28, pp. 2641–2650, 1989.

[13] J. R. Fienup, "Iterative method applied to image reconstruction and to computer-generated holograms," *Opt. Eng.*, vol. 19, pp. 297–305, 1980.

[14] D. C. Ghiglia and M. D. Pritt, *Two-Dimensional Phase Unwrapping: Theory, Algorithms, and Software.* New York: Wiley Interscience, 1998.

[15] D. L. Fried and J. L. Vaughn, "Branch cuts in the phase function," *Appl. Opt.*, vol. 31, pp. 2865–2882, 1992.

[16] D. L. Fried, "Branch point problem in adaptive optics," *J. Opt. Soc. Am. A*, vol. 15, pp. 2759–2768, 1998.

[17] R. R. Beland, "Propagation through atmospheric optical turbulence," in *IR/EO Handbook* (F. G. Smith, ed.), vol. 2, pp. 157–232, Bellingham, WA: SPIE Press, 1993.

[18] L. C. Andrews and R. L. Phillips, *Laser beam propagation through random media.* Bellingham, WA: SPIE Press, 1998.

[19] J. M. Martin and S. M. Flatte, "Simulation of point-source scintillation through three-dimensional random media," *J. Opt. Soc. Am. A*, vol. 7, pp. 838–847, 1990.

[20] J. M. Martin and S. M. Flatte, "Intensity images and statistics from numerical simulation of wave propagation in 3-d random media," *Appl. Opt.*, vol. 27, pp. 2111–2126, 1988.

[21] M. C. Roggemann and T. J. Schulz, "Algorithm to increase the largest aberration that can be reconstructed from hartmann sensor measurements," *Appl. Opt.*, vol. 37, pp. 4321–4329, 1998.

[22] V. I. Tatarskii, *The effects of the turbulence atmosphere on wave propagation.* Springfield, VA: US Department of Commerce, National Technical Information Service, TT68-50464, 1971.

[23] S. Enguehard and B. Hatfield, "Compensated atmospheric optics," *Prog. Quant. Electr.*, vol. 19, pp. 239–301, 1995.

[24] J. W. Goodman, *Introduction to Fourier Optics, Second Edition.* New York: McGraw-Hill Book Co., 1996.

[25] R. C. Gonzalez and R. E. Woods, *Digital Image Processing.* Reading, MA: Addison-Wesley, 1993.

[26] J. D. Gaskill, *Linear Systems, Fourier Transforms, and Optics.* New York: John Wiley & Sons, 1978.

[27] J. R. Fienup, J. C. Marron, R. G. Paxman, T. J. Schulz, J. H. Seldin, and B. J. Thelen, "Image inversion analysis of the hubble space telescope," Tech. Rep. 232600-15-F, Environmental Research Institute of Michigan, Ann Arbor, MI, 1991.

[28] D. A. Pierre, *Optimization Theory with Applications.* New York: Dover, 1986.

[29] M. A. Branch and A. Grace, *MATLAB Optimization Toolbox.* 24 Prime Park Way, Natick, MA: The Math Works, 1996.

[30] S. M. Flatte, G. Y. Wang, and J. M. Martin, "Irradiance variance of optical waves through atmospheric turbulence by numerical simulatino and comparison with experiment," *J. Opt. Soc. Am. A*, vol. 10, pp. 2363–2370, 1993.

[31] T. Goldring and L. Carlson, "Analysis and implementation of non-kolmogorov phase screens appropriate to structured environments," in *SPIE proceedings on Nonlinear Optical Beam Manipulation and High Energy Beam Propagation Through the Atmosphere*, vol. 1060, pp. 244–264, 1989.

[32] B. L. McGlamery, "Restoration of turbulence-degraded images," *J. Opt. Soc. Am.*, vol. 57, pp. 293–297, 1966.

[33] L. Zhu, P.-C. Sun, D.-U. Bartsch, W. R. Freeman, and Y. Fainman, "Adaptive control of a micromachined continous-membrane deformable mirror for aberration compensation," *Applied Optics*, vol. 38, pp. 168–176, 1999.

[34] G. Vdovin, "Micromachined adaptive mirrors," tech. rep., Laboratory of Electronic Instrumentation, Delft University of Technology, P.O.Box 5031, 2600 GA, Delft, The Netherlands, 1996.

[35] G. Vdovin, "37-channel micromachined adaptic optical system: technical report (control electronics + devices m4 and m5)," tech. rep., OKO Technologies, Reinier de Graafweg 300, 2625 DJ Delft, The Netherlands, 1998.

[36] R. C. Gonzalez and R. E. Woods, *Digital Image Processing.* Addison-Wesley, 1992.